

A New Cepheid Distance to the Giant Spiral M101 Based On Image Subtraction of HST/ACS Observations

Benjamin J. Shappee^{1,2}, and K. Z. Stanek¹

shappee@astronomy.ohio-state.edu, kstanek@astronomy.ohio-state.edu

October 23, 2018

ABSTRACT

We accurately determine a new Cepheid distance to M101 (NGC 5457) using archival HST/ACS V and I time series photometry of two fields within the galaxy. We make a slight modification to the ISIS image subtraction package to obtain optimal differential light curves from HST data. We discovered 827 Cepheids with periods between 3 and 80 days, the largest extragalactic sample of Cepheids observed with HST by a factor of 2. With this large Cepheid sample we find that the relative distance of M101 from the LMC is $\Delta\mu_{\text{LMC}} = 10.63 \pm 0.04$ (random) ± 0.07 (systematic) mag. If we use the geometrically determined maser distance to NGC 4258 as our distance anchor, the distance modulus of M101 is $\mu_0 = 29.04 \pm 0.05$ (random) ± 0.18 (systematic) mag or $D = 6.4 \pm 0.2$ (random) ± 0.5 (systematic) Mpc. The uncertainty is dominated by the maser distance estimate (± 0.15 mag), which should improve over the next few years. We determine a steep metallicity dependence, γ , for our Cepheid sample through two methods, yielding $\gamma = -0.84 \pm 0.22$ (random) ± 0.07 (systematic) mag dex⁻¹ and $\gamma = -0.72_{-0.22}^{+0.20}$ (random) ± 0.06 (systematic) mag dex⁻¹. We see marginal evidence for variations in the Wesenheit P-L relation slope as a function of deprojected galactocentric radius. We also use the TRGB method to independently determine the distance modulus to M101 of $\mu_0 = 29.05 \pm 0.06$ (random) ± 0.12 (systematic) mag.

Subject headings: Cepheids — distance scale — galaxies: individual (M101)

1. Introduction

Hubble Space Telescope (HST) observations of Cepheid variables have proven to be invaluable for extragalactic distance estimates outside the local group, determining distances out to ~ 35 Mpc (e.g. Freedman et al. 2001; Riess et al. 2009a,b). Type Ia supernovae and other secondary distance indicators used at greater distances rely on calibrations using extragalactic Cepheid distances.

¹Department of Astronomy, Ohio State University, Columbus, OH 43210, USA

²NSF Graduate Fellow

Through these calibrations, measurements of the Hubble constant (H_0) depend directly on the uncertainties in the Cepheid distance anchor. Utilizing the Wide Field and Planetary Camera 2 (WFPC2) aboard HST, the HST Key Project (Freedman et al. 1994, 2001) and the Supernova Ia HST Calibration Program (Saha et al. 2001; Sandage et al. 2006) were both able to determine H_0 with $< 10\%$ uncertainties. The two projects found estimates of $H_0 = 72 \pm 8 \text{ km s}^{-1} \text{ Mpc}^{-1}$ and $H_0 = 62.3 \pm 1.3$ (random) ± 5.0 (systematic) $\text{km s}^{-1} \text{ Mpc}^{-1}$, respectively, and the measurements were only consistent at the 2-sigma level.

A dominant source of systematic error for both these measurements is their dependence on the distance to the Large Magellanic Cloud (LMC) for the absolute calibration of the Cepheid distances. The distance to the LMC is only known to a precision of $\sim 10\%$, with some estimates differing by ± 0.25 mag (e.g. Benedict et al. 2002). With such a large uncertainty in the distance, it is important to replace the LMC as our extragalactic distance anchor. There have been some attempts to provide a replacement anchor, for example the eclipsing binary distance to M33 of Bonanos et al. (2006). NGC 4258, with a geometrically determined maser distance (Herrnstein et al. 1999), is one of the most promising alternatives to the LMC. Macri et al. (2006) used HST and the Advanced Camera for Surveys/Wide Field Camera (ACS/WFC; Ford et al. 2003) observations of Cepheids in NGC 4258 to make the maser host galaxy a viable distance anchor for extragalactic Cepheid distance measurements.

Extragalactic Cepheid distance measurements assume the Cepheids are at a common distance and apply the period-luminosity (P-L) relation of Cepheids variables. These measurements are complicated by the compositional dependence of the Cepheid P-L relation. The magnitude of this metallicity dependence has been under debate for over two decades with conflicting claims from theory (Stothers 1988; Stiff 1990; Fiorentino et al. 2002; Valle et al. 2009) as well as Galactic and extragalactic observations (Caldwell & Coulson 1986, 1987; Freedman & Madore 1990; Gould 1994; Stiff 1995; Sasselov et al. 1997; Kochanek 1997; Kennicutt 1998; Groenewegen et al. 2004; Sakai et al. 2004; Macri et al. 2006). Furthermore, Tammann et al. (2003) and Sandage & Tammann (2008) (and references therein) argued that the slope and zero-point of the P-L relation must be dependent on metallicity, although Madore et al. (2009) demonstrated that the slope of the “reddening free” Wesenheit P-L relation is insensitive to changes in the slope of the underlying V and I P-L relations. Riess et al. (2009b) do not see any dependence in the slope of fit Wesenheit P-L relations in a sample of 7 galaxies observed with WFPC2 and ACS/WFC with average metallicities spanning 0.2 dex.

The purpose of this paper is to measure the distance to M101 and test the universality of the Wesenheit P-L relation. We employ ISIS image subtraction (Alard & Lupton 1998; Alard 2000) on archival F555W and F814W time series ACS/WFC data of M101 to identify a large sample of Cepheids. Using NGC 4258 as our distance anchor we are then able to measure the distance to M101. With our large sample of Cepheid variables we explore possible variations in the slope and zero-point of the Wesenheit P-L relation as a function of deprojected galactocentric radius. We investigate the possibility of a constant slope and zero-point, a linearly varying zero-point with a

constant slope, a linearly varying slope with a constant zero-point, and a linearly varying slope and zero-point.

The paper is organized as follows: Section 2 describes the observations; Section 3 details the data reduction and image subtraction; Section 4 explains our Cepheid search algorithms; Section 5 presents our Cepheid distance to M101; Section 6 investigates the universality of the Wesenheit P-L relation with deprojected galactocentric radius; Section 7 presents our Tip of the Red Giant Branch (TRGB) distance to M101; Section 8 shows interesting non-Cepheid variable objects; Section 9 discusses our results; and Section 10 presents our six main conclusions.

2. Observations

For this work we used archival ACS/WFC data (GO program 10918; PI Wendy Freedman) of M101 (NGC 5457). M101 has been classified as a SAB(rs)cd III-IV spiral galaxy (de Vaucouleurs et al. 1991) and a S(s)c I spiral galaxy (Sandage & Tammann 1981). The images were first processed by the STScI ACS calibration pipeline (see Pavlovsky et al. 2005). We obtained the calibrated and flat-fielded images (`_flt.fits`) and the drizzled images (`_drz.fits`) from the Space Telescope Science Institute (STScI) HST Archive. The program observed two fields in M101 with Field 1 centered at $(\alpha, \delta) = (14^{\text{h}}03^{\text{m}}28^{\text{s}}.8, +54^{\circ}21'35''.0)$ and Field 2 centered at $(14^{\text{h}}02^{\text{m}}51^{\text{s}}.0, +54^{\circ}20'22''.0)$. Fig. 1 shows the position of these two fields as well as the WFPC2 fields used in the Hubble Key Project superimposed on the Sloan Digital Sky Survey (SDSS) image of M101 obtained using the Hubble Legacy Archive.¹

The fields were observed in both F555W (*V*-band) and F814W (*I*-band) for 12 epochs following a power law sampling in time to minimize possible period aliasing (Freedman et al. 1994; Madore & Freedman 2005). The observations have a baseline of ≈ 30 days and were completed between 2006 Dec 23 and 2007 Jan 21 (Field 1) and between 2006 Dec 25 and 2007 Jan 23 (Field 2). Table 1 provides a log of the observations. The observations were taken in a two point dither pattern with total exposure times at each epoch of 1330s for F555W and 724s for F814W.

3. Data Reduction

To make the most of these excellent data, we reduced them using a procedure that took advantage of both the increased sensitivity to variability that image subtraction provides and the high photometric precision inherent in instrument-dedicated photometry packages, such as the ACS module of the DOLPHOT package. Surprisingly, image subtraction has been underutilized on HST data even though it is well established in variable object searches at a variety of wavelengths (e.g.

¹<http://hla.stsci.edu/>

Henderson et al. 2010; Khan et al. 2010; Kozłowski et al. 2010; Nataf et al. 2010; Peeples et al. 2007; Wozniak 2000). Additionally, Bonanos & Stanek (2003) demonstrated the advantage of using image subtraction over more conventional photometric procedures in Cepheid variable observations, finding a nine-fold increase in the number of Cepheids found in Very Large Telescope observations of M83. To our knowledge, this work is the first paper applying image subtraction to HST data although the idea is not novel (Bersier 2001). The method we describe below uses image subtraction to produce light curves for all objects in our field in the instrumental magnitude system. We then use the ACS module of the DOLPHOT package to measure and correct the magnitudes of these sources to the Landolt (1992) V and I magnitude system.

3.1. Image Subtraction

We used the image-subtraction package ISIS² (Alard & Lupton 1998; Alard 2000). ISIS performs image subtraction utilizing a spatially variable kernel, allowing for accurate differential photometry even in crowded fields.

Before we ran ISIS, we used standard IRAF³ routines to multiply the drizzled images downloaded from the HST archive by their exposure time to change their units from flux to counts so that we can accurately determine the uncertainties in the photometry. We then interpolated individual frames to a single drizzled image in each field, so all exposures had the same astrometric positions. This is usually done with ISIS, but ACS data is especially difficult as it has large numbers of resolved sources. ISIS was originally developed for microlensing and assumes that all sources are point sources. Instead we used Sexterp (Sivard 2011, in preparation)⁴, a hybrid code which utilizes the interpolation method of ISIS with source identification and centroiding done by SExtractor (Bertin & Arnouts 1996). Using Sexterp we interpolated all the images to match the first F814W image in each field (j9o401010_drz.fits for Field 1 and j9o413010_drz.fits for Field 2). As a result, all of our quoted astrometric coordinates will be referenced to the header astrometry of these two images.

We used ISIS to create a reference image for each band in each field. First, ISIS transforms all the images to the same point-spread function (PSF) and background level by convolving the images with a space-varying convolution kernel. ISIS then stacks the resulting images using a 3-sigma rejection limit from the median. Fig. 2 and Fig. 3 show color composite images of the F555W and F814W reference images.

We then used DAOPHOT and ALLSTAR (Stetson 1987, 1992, 1994) for photometry on the

²The ISIS package and a tutorial are available at <http://www2.iap.fr/users/alard/package.html>.

³IRAF is distributed by the National Optical Astronomy Observatories, which are operated by the Association of Universities for Research in Astronomy, Inc., under cooperative agreement with the NSF.

⁴<http://www.astronomy.ohio-state.edu/~sivard/soft/is3/index.html>

four ISIS reference images, to find more than 250,000 objects on each image. We then matched objects in each field between the two filters and found that 142,018 and 160,551 matched in Field 1 and Field 2 respectively.

We next used ISIS to subtract each individual epoch from the corresponding reference image by first convolving the reference image with a space-varying kernel to match it to the image before subtracting it. In these subtracted images, all constant sources will disappear, leaving only the variable objects. ISIS makes a variability image by taking the mean absolute deviation of the subtracted images. A small region of the reference image and the variability image are shown in Fig. 4.

We then used ISIS to extract the light-curves of all the sources identified in the reference images by DAOPHOT. However, the resolved sources inherent in HST observations cause ISIS to make a poor PSF itself. Instead we fed ISIS the PSF created in DAOPHOT using carefully selected isolated stars. This procedure requires a slightly altered version of ISIS that we describe in Appendix A. Using this model PSF, we performed photometry on all the objects matched between the filters on all the subtracted images. ISIS outputs the light curves in differential flux units which we convert to an instrumental magnitude system using VARTOOLS (Hartman et al. 2008).

3.2. DOLPHOT magnitude calibration

The ACS module for DOLPHOT 1.1⁵ was used on the calibrated and flat-fielded images of M101 following to the recommended settings in the DOLPHOT User’s Guide⁶ and DOLPHOT ACS User’s Guide⁷. Photometry for each epoch and each field was performed separately with the same astrometric reference images as were used for ISIS. The recommended cuts were applied to remove non-stellar detections and to eliminate objects with uncertain photometry. For each epoch, we only accepted objects for which DOLPHOT reported a magnitude in both filters. After these cuts, DOLPHOT reported $\approx 320,000$ objects in Field 1 and $\approx 380,000$ objects in Field 2 for each epoch.

The output of DOLPHOT contains an instrumental and transformed magnitude for each filter as well as measurements for each of the individual, dithered frames. We used the combined transformed magnitudes for each filter. The final magnitudes are corrected for charge transfer efficiency (CTE) losses. DOLPHOT uses transformations given in Sirianni et al. (2005) to transform from the HST filters F555W and F814W to the Landolt (1992) V and I magnitudes. However, Sirianni et al. (2005) warn that these transformations have a large uncertainty and that theoretical

⁵<http://purcell.as.arizona.edu/dolphot/>

⁶<http://purcell.as.arizona.edu/dolphot/dolphot.ps.gz>

⁷<http://purcell.as.arizona.edu/dolphot/dolphotACS.ps.gz>

and empirical transformations differ. Unfortunately, these transformations are required to make use of any published Cepheid P-L relations. Many systematic biases can be avoided when using the maser-host galaxy NGC 4258 as a distance anchor, since the Macri et al. (2006) Cepheid sample was also observed with HST ACS/WFC and applied the same transformations. In such comparisons these photometric issues cancel.

To calibrate the light curves from image subtraction, we matched the DAOPHOT objects to DOLPHOT objects in each epoch, making sure to note the offset in positions due to the differing coordinate conventions between the two packages. We accepted DAOPHOT objects that matched an object in at least 1 DOLPHOT epoch, leaving 130,522 objects in Field 1 and 141,817 objects in Field 2. Differences between the DOLPHOT transformed magnitudes and ISIS instrumental magnitudes were then calculated individually for each object at each epoch where DOLPHOT had a matching object. We then used a weighted mean with iterative sigma clipping to find the magnitude offset for each object. Finally, each light curve was calibrated with the addition of this offset magnitude. Uncertainties in this offset were then added in quadrature to the Cepheid template fit mean magnitudes presented in §4.2.

Table 2 contains the positions and the calibrated V and I magnitudes of bright non-variable secondary standards. The magnitudes were measured on the first epoch for each field.

4. Cepheid Variable Search

In the following subsections we describe our variability search and Cepheid selection criteria, which is similar to that of Macri et al. (2006) and Riess et al. (2009b). A variability index is first used to drastically cut the number of sources. Light curves are then fit with a Cepheid template and poor fits are determined by an F-test and rejected. The Udalski et al. (1999a) P-L relations were adopted and color cuts applied to refine the Cepheid sample. Lastly, a minimum period cut and an iterative distance modulus fit removed Population II Cepheids and other outliers.

4.1. Variability Search

The Welch & Stetson (1993) variability index I_V was calculated on each of the light curves. The variability index is given by,

$$I_V = \sqrt{\frac{1}{n(n-1)} \sum_{i=1}^n \delta V_i \delta I_i} \quad (1)$$

where δV_i and δI_i are the residuals from the mean V and I magnitudes normalized by measurement uncertainties. Correlated deviations from the mean magnitude will contribute positively to the variability index whereas anti-correlated deviations contribute negatively. Thus, a constant star with random noise will have a variability index of ≈ 0 and a truly variable object will have a

positive variability index. Fig. 5 shows the variability index as a function of V magnitude for Field 1. We then selected objects with $I_V > 1.5$ as variable objects. Lastly, we removed objects with mean $(V - I) < 0$ mag and mean $(V - I) > 2.5$ mag. These color cuts are well outside the expected range of the instability strip and lessen the number of variable objects that had to be fit with a Cepheid template.

4.2. Cepheid Template Fit and F-Test

We then fit the Cepheid templates of Yoachim et al. (2009) to the variability-selected light curves from §4.1. The Yoachim et al. (2009) templates are a principle component analysis of a Fourier decomposition of Galactic Cepheids (Ochsenbein et al. 2000; Berdnikov 1997; Berdnikov & Turner 2001; Gieren 1981; Moffett & Barnes 1984; Coulson & Caldwell 1985; Berdnikov & Turner 1995; Henden 1996; Barnes et al. 1997), LMC Cepheids and SMC Cepheids (Udalski et al. 1999a,b; Sebo et al. 2002; Moffett et al. 1998). Yoachim et al. (2009) provides⁸ an Interactive Data Language (IDL) procedure to fit these Cepheid templates to light curves. As the amplitudes of different Cepheids with the same period are known to vary (Stetson 1996), we modified the IDL Cepheid code to allow the amplitude of the Cepheid templates to vary by a multiplicative factor. Naively, one would allow the first principle component of the Cepheid template to be left as a free parameter in the fit, as the majority of this component is amplitude variations (Yoachim et al. 2009). However, we found that even when bounded to values within the scatter seen in Figure 8 of Yoachim et al. (2009), this resulted in unrealistic Cepheid light curve fits.

The Cepheid fitting code implemented the IDL Levenberg-Marquardt least-squares minimization procedure `mpfit.pro`⁹ (Markwardt 2009) to fit the light curves giving an initial period and an initial phase. We started the fitting procedure at the two periods identified by the Minimum String Length Method (Burke et al. 1970; Dworetzky 1983) for the V and I light curves. However, no periodicity searching method will work for time baselines longer than the observational baseline. Fortunately, the accuracy of HST photometry and the use of Cepheid templates allows us to determine the properties of Cepheid variables with periods significantly longer than this baseline. This requires a brute force template fitting search for periods longer than the baseline. In addition to the Minimum String Length periods, we also tried 250 initial periods from 3–100 days logarithmically spaced for each Cepheid. The lowest initial period bound of 3 days we set because Cepheids with shorter periods would be too close to our detection limit to be useful. We set an upper bound of 100 days in the initial periods to avoid the possible change in the P-L relation as shown in Bird et al. (2009) for ultra-long period Cepheids. For each initial period we tried 10 different initial phases of the Cepheid template. We accepted the overall best-fit template for each variable based on the fit’s χ^2 value. Our method is computationally expensive but thorough. Representative light curves

⁸http://www.astro.washington.edu/users/yoachim/Ceph_code.tar.gz

⁹Available at <http://www.physics.wisc.edu/~craigm/idl/fitting.html>

for Cepheids in our final sample (as described in §4.4) are shown in Fig. 6 and Fig. 7 for Field 1 and Field 2 respectively.

We then performed a version of the F -test to reject non-Cepheid variable objects. We compared the χ^2/dof of the Cepheid template fit ($\chi^2/\text{dof}_{\text{template}}$) with that of a constant magnitude least-squares fit ($\chi^2/\text{dof}_{\text{constant}}$) and a linear least-squares fit ($\chi^2/\text{dof}_{\text{linear}}$) for both V and I light curves. We then define,

$$F = \frac{\min(\chi^2/\text{dof}_{\text{constant}}, \chi^2/\text{dof}_{\text{linear}})}{\chi^2/\text{dof}_{\text{template}}}. \quad (2)$$

A stringent $F > 3$ cut was then applied. Fig. 8 shows the distribution of F as a function of fit period for Field 1. The objects that survive this cut are the Cepheid candidates presented in Tables 3 and 4 along with their positions, variability index, fit period, fit mean magnitude and fit amplitudes.

4.3. Fiducial Period-Luminosity Relations

We adopted the updated OGLE-II P-L relations (Udalski et al. 1999a) (as updated on the OGLE website¹⁰) which have been the standard choice in most extragalactic studies (e.g. Freedman et al. 2001; Macri et al. 2006). Because we used the distance modulus to the LMC determined from the maser host NGC 4258 presented in Macri et al. (2006), we adopted the same P-L relation for our final distance measurement. This choice prevents possible systematic errors that could be caused by the adoption of a different P-L relation. The Udalski et al. (1999a) P-L relations were calculated on a sample of ≈ 650 Cepheids in the LMC, and are given by:

$$V_0 = 14.287(0.021) - 2.779(0.031) [\log P - 1] \quad (3)$$

$$I_0 = 13.615(0.014) - 2.979(0.021) [\log P - 1] \quad (4)$$

where P is the Cepheid period in days. We can then define the V and I LMC relative distance modulus:

$$\Delta\mu_V = V - V_0, \quad \text{and} \quad \Delta\mu_I = I - I_0 \quad (5)$$

where V and I are the measured Cepheid magnitudes. We then create the fiducial Cepheid color:

$$(V - I)_0 = V_0 - I_0 \quad (6)$$

using the adopted P-L relations. We can now define the color excess,

$$E(V - I) = (V - I) - (V - I)_0. \quad (7)$$

The LMC relative Wesenheit distance modulus (Madore 1982) is,

$$\Delta\mu_{\text{LMC}} = \Delta\mu_I - (R - 1)E(V - I). \quad (8)$$

¹⁰[ftp://sirius.astrouw.edu.pl/ogle/ogle2/var_stars/lmc/cep/catalog/README.PL](http://sirius.astrouw.edu.pl/ogle/ogle2/var_stars/lmc/cep/catalog/README.PL).

where $R \equiv A_V/(A_V - A_J)$. Finally, assuming a selective to total extinction coefficient $R_V = 3.1$, and using the A_λ from Table 6 of Schlegel et al. (1998) we calculate $R = 2.45$.

4.4. Selection Criteria and Final Sample of Cepheid Variables

We made the following cuts to our Cepheid candidate sample to identified true Cepheid variables and to minimize the effects of blending and extinction. We chose these cuts following the criteria of Macri et al. (2006).

(1) *Amplitude ratios* - Objects with a ratio of I amplitude to V amplitude greater than 0.75 or less than 0.25 were removed from the sample.

(2) *Blue blends* - Objects with $E(V - I) < 2\sigma$ below the Galactic foreground extinction value were removed from the sample. Cepheids that appear significantly bluer than the Galactic extinction are likely to have blue blends. We adopted $E(B - V) = 0.009$ mag or equivalently $E(V - I) = 0.011$ mag (Schlegel et al. 1998) as our foreground extinction.

(3) *Red blends and highly extinguished objects* - Objects with $E(B - V) > 0.5$ mag or equivalently $E(V - I) > 0.68$ mag were removed from the sample. Cepheids that appear extremely red are either highly extinguished or have red blends. Although the Wesenheit magnitude and Wesenheit distance modulus are resistant to reddening, highly extinguished sources may systematically differ if the true R_V value differs from our assumed R_V value. Additionally, if the color excess is due to blends these objects would clearly bias our distance.

(4) *Population II Cepheids* - Objects with a distance modulus relative to the LMC of $\Delta\mu_{\text{LMC}} > 11.5$ were removed from the sample to exclude W Virginis and RV Tauri variables. These Population II Cepheids have similar light curve shapes and colors as those of fundamental mode Cepheids, and some would have passed our initial sample selection.

(5) *Period Cut* - Object with a period < 3 days were removed from the sample because their light curves are too noisy for accurate identification of Cepheid candidates.

(6) *Iterative Sigma Clipping* - We then computed a weighted median LMC-relative distance modulus for each field using a least-absolute-deviation technique as also applied by Macri et al. (2006). We perform iterative sigma clipping to remove outliers. This weighted median was used in place of the typical mean modulus because of its outlier resistance. Additionally, any Cepheid distance moduli distribution is skewed due to blending and the median will be a more robust statistic against these systematic problems. The difference between these two fitting methods is investigated in §5.1.

The effects of the sample cuts are shown in Table 5. A period histogram for the final Cepheid sample is shown in Fig. 9. Cepheids and rejected Cepheids candidates are listed in Tables 3 and 4, respectively. The quantities derived using our fiducial PL for the final Cepheid sample are listed

in Table 6. The locations of the Cepheids are shown in Fig. 10 and Fig. 11 for Fields 1 and 2, respectively. The color-magnitude diagrams (CMDs) of the fields with the Cepheids marked are presented in Fig. 12. The V , I and W luminosities for the final Cepheid sample are shown as functions of period with the predicted Wesenheit P-L relation overlain are shown in Fig. 13. Finally, the V , I and W LMC-relative distance moduli are shown as a functions of period in Fig. 14.

5. The Cepheid Distance to M101

In the following subsections we describe how we determined the distance modulus of M101 from our Cepheid sample. We first refined our Cepheid sample through cuts in period and color. We then assume the Bresolin (2007) oxygen abundance gradient for M101 and compute the metallicities of our Cepheid sample. The distance modulus relative to the LMC was taken to be the distance modulus at $[O/H] = 8.50$ dex of a linear least-squares fit to the individual Cepheid distance moduli as a function of metallicity. Finally, we adopted the Macri et al. (2006) LMC distance modulus, which was determined from the Herrnstein et al. (1999) NGC 4258 maser distance, to compute our final distance modulus to M101.

5.1. Refined Cepheid Sample for Distance Determination

Because our goal is to determine the most accurate distance to M101, we require a refined sample of fundamental mode Cepheids. First, we exclude Cepheids with periods below 6 days because we are unable to distinguish between overtone and fundamental mode pulsators with such sparsely sampled light curves. Overtone pulsators with periods < 6 days have similar light curve shapes but are significantly brighter than their fundamental mode counterparts (e.g. Udalski et al. 1999a), and thus would bias our distance measurement.

We computed the median distance modulus relative to the LMC under minimum period cuts from 6 to 20 days following the procedure described in §4.4. This analysis is similar to the period cuts performed in §4.2.1 of Macri et al. (2006) and we share the motivation therein. Fig. 15 shows the median distance moduli relative to the LMC as a function of the minimum period for Fields 1 and 2. We find that lower period cutoffs lead to smaller distance moduli. To avoid this bias, we adopt a minimum period of 14 days for both fields. Fig. 16 and Fig. 17 show the distance modulus relative to the LMC as a function of period for Fields 1 and 2, respectively. Fig. 18 and Fig. 19 show the $E(V-I)$ color excess as a function of period for Field 1 and Field 2 respectively. These four plots also show the rejected Cepheid candidates from Table 4 for reference. These period cuts lead to a median distance modulus relative to the LMC of $\Delta\mu_{\text{LMC}} = 10.58 \pm 0.01$ mag using 155 Cepheids in Field 1 and $\Delta\mu_{\text{LMC}} = 10.57 \pm 0.02$ mag based on 135 Cepheids in Field 2. For each of the minimum period cuts, we also show the difference between the mean and median fit distance moduli relative to the LMC in Fig. 20. At a period cut of 14 days, there is a small difference in

the distance moduli 0.03 ± 0.01 mag and 0.03 ± 0.02 mag for Fields 1 and 2, respectively.

For our final distance measurement Cepheid sample we make more stringent cuts than were performed in §4.4 as were also applied by Macri et al. (2006) to remove blue blends, remove red blends and ensure that our sample cover the same range in extinction. We discard Cepheids with color excesses below the Galactic foreground reddening $E(B - V) < 0.011$ mag, or, equivalently, $E(V - I) < 0.015$ mag. We also remove Cepheids that show large reddening, $E(B - V) > 0.28$ mag, or, equivalently, $E(V - I) > 0.39$ mag, leaving 235 Cepheids in our refined Cepheid sample.

5.2. Deprojection and Metallicity Dependence

Extragalactic Cepheid studies make the implicit assumption that the galactic oxygen abundance gradient tracks the metallicity of Cepheids at the same galactocentric radius. With this assumption we obtain a differential measurement of the metallicity dependence of the Wesenheit P-L relation. M101 displays one of the strongest radial abundance gradients found among nearby spiral (Kennicutt & Garnett 1996). We adopted the following oxygen abundance gradient for M101 from Eq. 5 in Bresolin (2007):

$$[\text{O}/\text{H}] = (8.75(0.05) - 0.90(0.07)\rho) \text{ dex} \quad (9)$$

where ρ is the fractional isophotal. Bresolin (2007) extended the 20 H II oxygen abundance measurements of Kennicutt et al. (2003) to within $1'5$ of the galactic center with two additional measurements in the inner regions of M101. Figure 2 of Bresolin (2007) shows the oxygen abundance gradient fit for M101 where the H II regions span more than a dex in metallicity. We then computed the deprojected galactocentric distances for the Cepheids were calculated using the following corrected¹¹ equations presented in Macri et al. (2006):

$$x = (\alpha - \alpha_0) \cos \delta_0 \cos \phi + (\delta - \delta_0) \sin \phi \quad (10)$$

$$y = \frac{(\delta - \delta_0) \cos \phi - (\alpha - \alpha_0) \cos \delta_0 \sin \phi}{\cos i} \quad (11)$$

$$\rho = \frac{(x^2 + y^2)^{\frac{1}{2}}}{R_0} \quad (12)$$

where R_0 is the isophotal radius. We adopted the nuclear position of M101 from Corwin et al. (1994) of (J2000) $(\alpha, \delta) = (14^h 03^m 12^s 53, +54^\circ 20' 55''.6)$. We also adopted the major axis position angle $\phi = 35^\circ 0 \pm 1^\circ 0$ and inclination of $i = 17^\circ 0 \pm 1^\circ 0$ from Zaritsky et al. (1990). Additionally, we assumed isophotal radius $R_0 = 14'.4$ from de Vaucouleurs et al. (1991) as was also assumed in Bresolin (2007). Finally, we computed the metallicities of the Cepheids in our final sample as reported in Table 6.

¹¹Eq. 11 and Eq. 12 in Macri et al. (2006) are missing the geometric factor of $\cos \delta_0$.

Fig. 21 shows the LMC relative distance modulus as a function of the deprojected galactocentric distance and metallicity for the refined Cepheid sample. A linear least-squares fit and a constant least-squares fit to the data are shown in Fig. 21. The standard deviation about the linear fit and the constant fit are 0.17 mag and 0.18 mag, respectively. The χ^2 values of the linear fit and constant fit are $\chi^2=1077.1$ and $\chi^2=1142.8$, respectively. We see that the linear least-squares fit is preferred by the data. Fig. 22 displays the residuals from the linear least-squares fit against $E(V - I)$, where no dramatic trends are seen.

A linear least-squares fit to the data yields a slope of $\gamma = -0.84 \pm 0.22_r \pm 0.07_s$ mag dex⁻¹ and a zero-point determination at $[O/H] = 8.50$ dex of $\Delta\mu_{\text{LMC}} = 10.63 \pm 0.02_r \pm 0.04_s$ mag¹². We determined the random uncertainties of the linear best-fit parameters by bootstrap re-sampling the Cepheids with 2.5×10^4 simulations. In each simulation we randomly re-sampled the refined Cepheid sample with replacement, to create a new sample with the same size. For each re-sample we calculated the linear least-squares best-fit slope and zero-point. We then took the standard deviation of the distribution of 2.5×10^4 best-fit slopes/zero-points as the random uncertainty in the original determined slope/zero-point, respectively. As both fields in the data are at approximately the same deprojected galactocentric distance, we have a relatively small range in metallicity with which to determine the correlation between metallicity and luminosity, leading to the large uncertainty we see in γ . The systematic uncertainties are calculated from the uncertainties in the Bresolin (2007) oxygen abundance gradient. The random and systematic uncertainties in the zero-point are included in the distance error budget shown in Table 7, represented by R5 and S4, respectively.

To test if the Cepheids at the smallest galactocentric radii dominated the linear least-squares fit, we removed Cepheids with metallicities less than 8.65 dex from our sample and refit. The new best-fit slope $\gamma = -0.66 \pm 0.25_r \pm 0.05_s$ mag dex⁻¹ is shallower but consistent with the slope determined before the metallicity cut. Even with a large uncertainty in γ there is tension (2.2σ) between our measured value and the Hubble Key Project determination of $\gamma = -0.24 \pm 0.16$ mag dex⁻¹ for M101 using WFPC2 data (Kennicutt 1998). The implications of our measured Cepheid metallicity dependence are discussed in §9.

5.3. Final Cepheid Distance to M101

We then adopted the Macri et al. (2006) LMC distance modulus $\mu_{\text{LMC}} = 18.41 \pm 0.10_r \pm 0.13_s$ mag determined from the Herrnstein et al. (1999) NGC 4258 maser distance to compute our final distance modulus to M101. Our error budget is shown in Table 7. We report a distance modulus relative to the LMC of $\Delta\mu_{\text{LMC}} = 10.63 \pm 0.04_r \pm 0.07_s$ mag and a M101 distance

¹²In this paper we denote random and systematic uncertainties with subscript r and s respectively, i.e., $3.00 \pm 0.10_r \pm 0.10_s$ mag.

modulus of $\mu_0 = 29.04 \pm 0.05_r \pm 0.18_s$ mag. We compare these distances to other determinations of distance modulus relative to the LMC and estimates of the distance to M101 in Table 8.

6. Slope and Zero-Point of the Wesenheit P-L Relation

We can also use the large number of extragalactic Cepheids in our sample to test the universality of the Wesenheit P-L relation. Let us define the classic “Wesenheit reddening-free” mean magnitude by:

$$W = V - R(V - I), \quad (13)$$

where R is defined in §4.3. Based on the mean V and I magnitudes of our final Cepheid sample given in Table 6 we can define an expected mean Wesenheit magnitude (W_0) for each Cepheid. We then want to fit for a Wesenheit P-L relation:

$$W_0 = a_w \log P + b_w \quad (14)$$

where the slope a_w and zero-point b_w may depend on deprojected radius as a proxy for metallicity. Based on Eq. 14, the expected mean Wesenheit magnitude as a function of period and ρ for each of these models is given by:

$$W_0(P) = [a_w^I + a_w^S(\rho - \rho')](\log P - \log P') + [b_w^I + b_w^S(\rho - \rho')] \quad (15)$$

where a_w^I and b_w^I are the values of the slope and zero-point, respectively, of the Wesenheit P-L relation at some characteristic fraction of the isophotal radius (ρ'). a_w^S and b_w^S are the rates at which the slope and zero-point of the Wesenheit P-L relation change with ρ . The zero-point of the Wesenheit P-L relation is defined at a characteristic pulsation period (P'). In order to minimize the covariance between a_w^I , a_w^S , b_w^I and b_w^S we use the mean log period ($\log P' = 1.3 \log(\text{days}) \approx \langle \log P \rangle$) and mean fractional isophotal radius ($\rho' = 0.2 \approx \langle \rho \rangle$) for the characteristic period and radius, respectively.

We use the Cepheid sample in Table 3 and imposed the same minimum period cut of $P > 14$ days used in §5.1 and either impose no maximum period cut or impose a maximum period cut of $P < 40.0$ days to define a full and restricted sample, respectively. There are two reasons a maximum period may avoid systematic deviations. First, the ≈ 30 day baseline of our data makes the period and magnitude determination suspect for very long period Cepheids. Many of them are missed in any case because they fail our F-test in §4.2. Eliminating the long period Cepheids is of little concern when determining the distance modulus to M101 because the mean magnitude and period errors will also be larger on these objects. However, our ability to estimate the radius-dependent slopes of the Wesenheit P-L relation could be strongly affected by the stochastic nature that the inclusion of a very few long period Cepheids would induce. However, adopting this maximum cut limits our sensitivity to changes in the P-L slope. As there is no obvious solution to address both concerns, we performed and present both fits. After trimming, there are 297 Cepheids in our full sample and 278 Cepheids in our restricted sample.

We then fit Eq. 15 to both the full and restricted samples using the following procedure. First, we fit a model with no radial dependence, and iteratively remove outliers. We took the 100 Cepheids closest in radius to each Cepheid, computed their scatter about the best-fit Wesenheit P-L, and rejected the Cepheid if it was more than 3 times the scatter from the best-fit P-L relation. This procedure takes into account the increased scatter of Cepheids at smaller ρ . We then renormalized the errors to have $\chi^2/\text{dof} = 1$ for the model with no radial dependence to account for the intrinsic scatter of the Cepheids. We then used the IDL Levenberg-Marquardt χ^2 minimization procedure `mpfit.pro` (Markwardt 2009) to fit four model Wesenheit P-L relations, Model 1 had a constant slope and zero-point, Model 2 had a linearly varying zero-point with a constant slope, Model 3 had a linearly varying slope with a constant zero-point and Model 4 had a linearly varying slope and zero-point. For each model initial a_w^I and b_w^I values were taken from the best-fit model with no radial dependence and the initial slopes a_w^S and b_w^S were taken to be 0. a_w^S and b_w^S were fixed to 0 for the constant slope models and the constant zero-point models, respectively. To determine the 68% confidence intervals for each model we performed a bootstrap re-sampling with 2.5×10^4 simulations. Fig. 23 and Fig. 26 present the Model 1, Model 2 and Model 4 fits on top of the Wesenheit P-L relations for six sub-samples with equal number of Cepheids stepping out in deprojected radius for the full and trimmed sample, respectively. The best-fit slope and best-fit zero-point, both as a function of ρ , for the full sample are shown in Figures 24 and 25, respectively. The best fit slope and intercepts of the six sub-samples in Fig. 23 are also shown for comparison in Figures 24 and 25, respectively. Best-fit parameters and χ^2 values for the four model are presented in Table 9. Using the Bresolin (2007) abundance gradient we transform these fit parameter into functions of metallicity as shown in Table 10. The characteristic radius is then equivalent to a characteristic metallicity of 8.57 dex.

We then compared the models and tested the validity of the additional terms between models fit to both samples. Based upon the χ^2 values presented in Table 9 the data seems to prefer models 2 and 4 over model 1 for both samples. We then computed the F-test confidence to quantify our justification for additional parameters between models 1 and 2 and between models 2 and 4. The calculated confidence levels are shown in Table 11. Both Cepheid samples are better fit by Model 2 than Model 1. This is expected because a changing Wesenheit P-L zero-point (b_w^S) is equivalent to the change in the distance modulus as a function of metallicity (γ) presented in Fig. 21. When comparing Model 2 and Model 4 we note a marginal detection of a change in the Wesenheit P-L relationship slope with ρ . This detection is at a 93.6% confidence level for the full sample, but the significance decreases to 89.4% for the restricted sample. We postpone further discussion until § 9.

7. TRGB Distance to M101

We also determined the distance to M101 using the TRGB method (Lee et al. 1993). The underlying physics of this method is well understood and described in Salaris et al. (2002). The effects of metallicity are also well understood (Bellazzini et al. 2001, 2004), and many methods

exist to correct for these effects (Mager et al. 2008; Madore et al. 2009). The TRGB method must be applied at the largest possible galactocentric radii to limit contamination from the intermediate mass asymptotic giant branch (AGB) stars (Sakai et al. 1996). AGB stars have a continuous distribution at similar colors but extend to higher luminosities than the TRGB, diluting the abrupt edge of the old, low mass stars at the TRGB.

The TRGB method works best given deep and accurate photometry. To accomplish this we reran DOLPHOT for each field, but include all epochs in a single run. DOLPHOT then combines each epoch’s photometry and computes one transformed magnitude per object per band. This second run of DOLPHOT yielded 3.75×10^5 and 3.90×10^5 sources in Fields 1 and 2, respectively. We then trimmed the sample for optimally application of our TRGB detection method. We first eliminated sources at galactocentric radii smaller than $4.75'$ to limit the contamination from AGB stars, yielding 5.64×10^3 and 3.69×10^4 sources from Fields 1 and 2, respectively. We removed sources with $V - I < 1.00$ mag as they are too blue to be TRGB stars. Our final TRGB sample size contained 2.65×10^3 and 2.22×10^4 sources from Fields 1 and 2, respectively.

We then applied reddening corrections to account for the small amount of foreground extinction. Based on the Schlegel et al. (1998) dust maps, the foreground absolute extinction correction of V and I are $A_V = 0.028$ mag and $A_I = 0.017$ mag.

We then used these corrected magnitudes to calculate the Madore et al. (2009) T magnitude for all our TRGB sources:

$$T \equiv I_o - \beta[(V - I)_o - \gamma_{\text{TRGB}}], \quad (16)$$

where β is the I versus $V - I$ slope of the TRGB, and γ_{TRGB} is the fiducial color where the T magnitudes are normalized to the I magnitude of a TRGB star of that color. The T magnitude is constructed to correct for the slope of the tip I magnitudes as a function of $V - I$, forcing the tip T magnitudes to be constant over a large range of colors or equivalently metallicities¹³. With the TRGB slant removed, edge detection methods more efficiently determine the TRGB position with fewer sources. Madore et al. (2009) adopt $\beta = 0.20 \pm 0.05$ for the intrinsic color range $1.5 < (V - I)_o < 3.0$, which is the color range observed for our TRGB. This slope is consistent with both observational values of $\beta = 0.22 \pm 0.02$ (Rizzi et al. 2007) and theoretical predictions of $\beta = 0.15$ (Mager et al. 2008). With a fiducial color of $\gamma_{\text{TRGB}} = (V - I)_o = 1.5$ mag, Madore et al. (2009) define the distance modulus based on the TRGB by:

$$\mu_{\text{TRGB}} \equiv T - M_{\text{TRGB}} = T + 4.05(0.12) \text{ mag}, \quad (17)$$

where M_{TRGB} is the TRGB absolute I magnitude at the fiducial color γ . The uncertainty in M_{TRGB} was taken from Mager et al. (2008), a companion paper to Madore et al. (2009). The absolute TRGB adopted in both Madore et al. (2009) and Mager et al. (2008) are 0.01 mag different at the same fiducial color, so we adopt the uncertainty presented in Mager et al. (2008).

¹³See Figure 1 in Madore et al. (2009) for a schematic representation.

The TRGB magnitude is determined using an edge detection procedure similar to that of Sakai et al. (2004), but using the newly constructed T magnitude in place of the typical I magnitude. A continuous luminosity function $\phi(m)$ was first computed using equation (A1) in the appendix of Sakai et al. (1996). We then used equation (4) of Méndez et al. (2002) to compute a logarithmic edge-detection response function $E(m)$. This function is a continuous version of a Sobel filter. Similar to what is done in discrete edge detectors, we weight the edge-detector response by the Poisson noise of our luminosity function, $E(m)[\phi(m)]^{\frac{1}{2}}$ (Méndez et al. 2002) and took the maximum as the TRGB. We then estimated the random uncertainty of tip determination by bootstrap re-sampling of the TRGB sample with 2.5×10^4 simulations. In each simulation we randomly re-sampled the TRGB sample with replacement to create a new sample of the same size. For each re-sample we determine the TRGB T magnitude with our edge detection method. We then took the standard deviation of the distribution of 2.5×10^4 TRGB T magnitudes as the random uncertainty in the original tip detection. Fig. 27 presents the T magnitude CMD in the left panel with the tip detection response function in the right panel. The tip detection at $T = 25.00 \pm 0.06$ mag is marked on both panels for reference. With this detection, we use Eq. 17 to determine the TRGB distance modulus of $\mu_0 = 29.05 \pm 0.06_r \pm 0.12_s$ mag. The systematic uncertainty is dominated by the uncertainty of M_{TRGB} .

8. Non-Cepheid Variable Objects

There have been many studies searching for luminous variable stars, including a recent study of the LMC which found 117 variable objects with absolute magnitudes of $M_V \gtrsim -4.4$ mag (Szczygiel et al. 2010). We performed a non-exhaustive (by eye) search of the brightest, most variable objects in both fields which are not in our final Cepheid sample shown in Table 3. The majority of these objects appeared to be rejected Cepheid candidates, which usually displayed an obvious reason for their rejection, namely blends from colors or luminosity. Additionally, many possible long period Cepheids were rejected since they had poor light curve coverage due to the restricted time span of the data.

Some of the most luminous and interesting variable objects are shown in Fig. 28 with their properties given in Table 12. Possible periodic objects are shown in Fig. 29 with their properties listed in Table 13. Fig. 30 presents the CMD of both fields with the luminous variables marked.

9. Discussion

In §5 and §7 we determined the distance to M101 using Cepheids and the TRGB method, respectively, and found that they are in good agreement with $\mu_{\text{Ceph}} = 29.04 \pm 0.05_r \pm 0.18_s$ mag and $\mu_{\text{TRGB}} = 29.05 \pm 0.06_r \pm 0.12_s$ mag. We compared our M101 distance moduli against other recent studies in Table 8. We see that our LMC relative distance modulus is in excellent agreement with

the recent measurements of Saha et al. (2006) and Freedman et al. (2001) and our absolute M101 distance moduli differ within the uncertainties. This difference is due to the applied luminosity calibration for the adopted Cepheid P-L relations. Saha et al. (2006) used a hybrid method to determine the metallicity dependence of the P-L relation determined using Galactic Cepheids from Tammann et al. (2003) and LMC Cepheids from Sandage et al. (2004). However, the Wesenheit P-L slopes measured for the seven galaxy sample of Riess et al. (2009b) are significantly shallower than the Wesenheit P-L slope of Tammann et al. (2003). Riess et al. (2009b) points out the many difficulties with the method of the Tammann et al. (2003) Galactic Cepheid P-L determination including the use of non-parallax based distances and high mean extinctions.

Despite our large sample of Cepheids, our M101 distance modulus measurement suffers from large systematic uncertainties. As seen in Table 7, the majority of this uncertainty originates from the Herrnstein et al. (1999) maser distance to NGC 4258. Efforts to improve the uncertainty of the maser distance to NGC 4258 to 3% are underway using Very Long Baseline Array observations (Argon et al. 2007; Humphreys et al. 2008). However, to our knowledge, Herrnstein et al. (1999) is the latest actual measurement in the literature. Table 7 contains a goal error budget calculated under the assumption of a 3% maser distance to NGC 4258. Additionally, as this is a differential measurement, systematic errors in the photometric calibrations could be negated with a reanalysis of the Macri et al. (2006) Cepheid observations of NGC 4258 with the same photometric procedure.

We note that the H_0 measurement with a total uncertainty of 4.8% from Riess et al. (2009a) uses the published maser distance of $\mu_{\text{N4258}} = 29.29$ mag from Herrnstein et al. (1999) but assumes the error bars (3%) of the yet unpublished result of Humphreys et al. (2009) rather than the published uncertainties (7%) of Herrnstein et al. (1999).

The universality of the Wesenheit P-L relation has been a point of concern and contention in the literature since it has important implications for deriving extragalactic distances. With our large sample of M101 Cepheids we investigate the Wesenheit P-L as a function of deprojected galactocentric radius, and by assumption, as a function of metallicity. We determine the metallicity dependence of the Wesenheit P-L zero-point in §5.2 and §6 to be $\gamma = -0.84 \pm 0.22_r \pm 0.07_s$ mag dex⁻¹ and $\gamma = b_w^S = -0.72^{+0.20}_{-0.22}(\text{random}) \pm 0.06_s$ mag dex⁻¹, respectively. These metallicity dependences are in contention with current values in the literature. Using the TRGB method as a metallicity independent distance indicator Sakai et al. (2004) report $\gamma = -0.25 \pm 0.09$ mag. However, the Sakai et al. (2004) results have recently been challenged in Rizzi et al. (2007). The HST Key Project reported $\gamma = -0.24 \pm 0.16$ mag dex⁻¹ (Kennicutt 1998) using an WFPC2 data for an inner field and an outer field in M101. There is even contention with the more recent determination from Macri et al. (2006) who found $\gamma = -0.29 \pm 0.09_r \pm 0.05_s$ mag dex⁻¹ using HST ACS data of NGC 4258. However, Bono et al. (2008) shows that by removing a single outlier H II region used in the determination of the metallicity gradients of NGC 4258 leads to a far shallower metallicity gradient:

$$[\text{O}/\text{H}] = (8.89 - 0.16(\rho - 0.4)) \text{ dex}, \quad (18)$$

then assumed by Macri et al. (2006):

$$[\text{O}/\text{H}] = (8.97 \pm 0.06) - (0.49 \pm 0.08)(\rho - 0.4) \text{ dex.} \quad (19)$$

With the shallower metallicity gradient of Bono et al. (2008), the γ measurement of Macri et al. (2006) for NGC 4258 steepens to $\gamma = -0.89 \text{ mag dex}^{-1}$, and is consistent with our estimate for M101.

There have been arguments that the change in the zero-point of the Wesenheit P-L as a function of deprojected galactocentric radius may be partially due to changes in blending as well as metallicity. For example, Bono et al. (2008) argues that blending could explain the negative values of γ that are seen because Cepheids in the inner region will be more blended on average, decreasing their apparent distance modulus. The idea that blending could undermine the community’s efforts to use Cepheids as a distance indicator has been discussed in many studies including Stanek & Udalski (1999), Mochejska et al. (2000) and Macri et al. (2001).

In addition to the varying zero-point of the Wesenheit P-L, the slope is also expected to show variations at some level. Sandage & Tammann (2008) argue that slope of the V -band P-L relation decreases monotonically with metallicity. However, Madore et al. (2009) show that the Wesenheit P-L slope is largely insensitive to changes in the slopes of the underlying monochromatic P-L relations. Through an algebraic argument and reasonable assumptions about the observed properties of Cepheids, Madore et al. (2009) show that the change in slope of the Wesenheit P-L could be ≈ -0.3 times the change in the slope of the V P-L. However, Madore et al. (2009) notes that the observational properties used are not currently known to a 10% precision, so their conclusions must be taken with caution.

Our Cepheid sample is marginally better fit by a Wesenheit P-L relation model with both slope and zero-point linearly varying as a function of deprojected isophotal radius than by a model with a linearly varying zero-point alone. The evidence for a linearly varying slope as a function of ρ degrades when using a sample with an applied maximum period cut of 40.0 days. However, this degradation was expected as the shortest and longest period Cepheids are those that best constrain the slope of the Wesenheit P-L. We see three possible explanations for our observations:

1. If Cepheid blending is a larger effect at smaller radii ρ , then one would naively expect a change in slope with our observed sign. To illustrate this point, imagine adding a constant flux to all Cepheids as a function of ρ ; one would then expect more than just a change in the zero-point of the Wesenheit P-L relation. At smaller ρ the less luminous, shorter period Cepheids would increase in magnitude more than their more luminous, longer period counterparts at the same ρ . Thus the slope of the Wesenheit P-L relation would become shallower in the inner regions of a galaxy. This type of blending is not trivial or obvious, as the smooth increase in the stellar density would simply be subtracted in our photometric procedures. An increase in stellar density associated with Cepheids as a function of ρ would have to be invoked. A detailed and quantitative analysis of the magnitude of this effect is beyond the scope of this study.

2. From the recent work of Sandage & Tammann (2008) and Madore et al. (2009), it is expected that the metallicity dependence of the Wesenheit P-L slope should be small. First, assume that the change in the slope of the Wesenheit P-L relation is a negative fraction of the change in the slope of the V P-L relation (Madore et al. 2009). Also assume that the V P-L slope decreases monotonically with metallicity (Sandage & Tammann 2008). From this we would expect the observed Wesenheit P-L relation to become shallower towards higher metallicities in the inner regions of a galaxy.

3. The observed change in slope of the Wesenheit P-L relation is tenuous, and as such could simply be a statistical fluctuation in the data.

M101 is a large face-on spiral galaxy, has bright H II regions at all radii and displays one of the strongest radial abundance gradients found among nearby spiral (Kennicutt & Garnett 1996), which makes it an extremely useful object to study the systematic effects on the Wesenheit P-L relation for Cepheids. The two fields observed in M101 used in this study are at approximately the same deprojected galactocentric radius, so the range in ρ is relatively small. This makes any study of the effects that ρ or metallicity have on the observed Wesenheit P-L relation difficult. It would be worth while to obtain another equivalent set of Cepheid observation of M101 at a greater deprojected galactocentric radius to further test the effects of metallicity on the Wesenheit P-L relation. Additionally, it would be useful and of relatively little cost to reobserve one of the fields in M101 used in this work for 2-3 additional epochs with HST/ACS. These observations would help to identify and constrain the periods of Cepheids with periods greater than 30 days. With a large sample of Cepheids covering a large range in period it would be possible to test the change in the P-L relation slope for Ultra Long Period Cepheids at periods > 100 days (Bird et al. 2009).

10. Summary

We accurately determine a Cepheid distance to M101 (NGC 5457) using archival HST ACS V and I time series photometry of two fields within the galaxy. We used ISIS image subtraction to obtain differential light curves and developed a new method where ISIS uses an externally determined PSF model. We used DAOPHOT to create this PSF model and DOLPHOT to calibrate the photometry. Our six primary results are:

1. We discovered 827 Cepheids using 12 epochs of HST ACS/WFC F555W and F814W data for two fields within M101.

2. We determine a Cepheid based LMC-relative distance modulus to M101 of $\Delta\mu_{\text{LMC}} = 10.63 \pm 0.04_r \pm 0.07_s$ mag if we assume the OGLE II LMC V -band and I -band PL relations.

3. Based on the Herrnstein et al. (1999) geometrically determined maser distance to NGC 4258 and the Macri et al. (2006) Cepheid based LMC-relative distance modulus to NGC 4258, we determine an absolute M101 distance modulus of $\mu_0 = 29.04 \pm 0.05_r \pm 0.18_s$ mag.

4. We also determine a M101 distance modulus based on the TRGB method of $\mu_0 = 29.05 \pm 0.06_r \pm 0.12_s$ mag.

5. We find a steep Cepheid metallicity dependence through 2 methods, yielding $\gamma = -0.84 \pm 0.22_r \pm 0.07_s$ mag dex⁻¹ and $\gamma = b_w^S = -0.72_{-0.22}^{+0.20}$ (random) $\pm 0.06_s$ mag dex⁻¹.

6. Our Cepheid sample is marginally better fit by a P-L relation where both the slope and the zero-point linearly vary with galactocentric radius, over models with only a linearly varying zero-point.

We would like to thank Christopher Kochanek, Lucas Macri, and Jennifer van Saders for their invaluable suggestions and discussions. We would also like to thank Joe Antognini, Thomas Beatty, Andrew Dolphin and Jill Gerke for other useful suggestions. This research gratefully made use of the NASA/IPAC Extragalactic Database (NED). Benjamin J. Shappee was supported by a Graduate Research Fellowship from the National Science Foundation.

A. Creating a PSF for ISIS from Daophot

Here we describe how to make ISIS use an externally determined PSF model.

Before creating the ISIS PSF from a DAOPHOT PSF we must first use IRAF to change the units and zero-point of the ACS/WFC drizzled images. We must have run the modified ISIS interp.csh¹⁴, the stock script ref.csh and the stock script subtract.csh to create the ISIS reference images and subtracted images.¹⁵ Additionally, DAOPHOT must be run on each reference image, carefully selecting a sample of PSF stars. Besides iteratively rejecting stars which differ from the DAOPHOT model PSF, we must also reject stars which have extended emission or objects with other stars nearby. Rejecting stars which have other nearby stars can be done using the WATCH PROGRESS option in DAOPHOT. We now have a PSF from DAOPHOT which is free of contamination from non-point sources which we save as PSF.fits. We also use standard procedures in DAOPHOT and ALLSTAR to create a catalog of source positions and photometry. We remove non-stellar sources from the catalog using cuts on the catalog. We then use the source list (.als) from ALLSTAR as an object list for ISIS by using the following awk command and removing the first 3 lines:

```
awk '{printf"%9.3f %9.3f %5.0f %5.0f %13s %8.3f %6.3f\n", $2-1, $3-1, $2-1, $3-1, "lc"$1".data", $4-0.1, $5}' ref.als > ! phot.data
```

¹⁴<http://www.astronomy.ohio-state.edu/~sivervd/soft/is3/index.html>

¹⁵The script detect.csh can also be run to create the stacked subtracted images seen in Fig. 4. However, these images are not used to obtain the differential flux light curves in our analysis.

where the -1 pixel shift in the awk command accounts for the difference in the coordinate conventions between DAOPHOT and ISIS¹⁶. This object list should be the file associated with the VARIABLES parameter in the ISIS process_config file.

We then need to manually make two files which ISIS usually creates and put them in the directory with the images to be processed by ISIS. The first is an $n \times n$ fits image named 'psf_file0.fits' filled with zeros, where n is specified by psf_width in the ISIS phot_config file. The second file must be named 'psf_table' which will contain one line of the form:

```
psf_file0.fits      9      9 4211 4234      0      0,
```

where the 1st element is the PSF file name, the 2nd and 3rd are the center of the 'psf_file0.fits' image in ISIS coordinates and the 4th and 5th are the x,y size of the reference images in pixels. We then use the addstar command in DAOPHOT to put a 'fake' star with extremely high signal to noise to the center of psf_file0.fits. It is important to account difference in the pixel coordinate system convention of DAOPHOT when creating the PSF.

Lastly, the stock phot.csh script must be altered so that it does not call the program Bphot, which would usually make the ISIS PSF. The modified phot.csh script can then be run, creating the light curves for every object in the object list created in DAOPHOT. These light curves will be in differential flux units, but can be transformed to an instrumental magnitude using 'fluxtomag' in the VARTOOLS¹⁷ package.

REFERENCES

- Alard, C. 2000, A&AS, 144, 363
- Alard, C., & Lupton, R. H. 1998, ApJ, 503, 325
- Argon, A. L., Greenhill, L. J., Reid, M. J., Moran, J. M., & Humphreys, E. M. L. 2007, ApJ, 659, 1040
- Barnes, III, T. G., Fernley, J. A., Frueh, M. L., Navas, J. G., Moffett, T. J., & Skillen, I. 1997, PASP, 109, 645
- Barnes, III, T. G., Jefferys, W. H., Berger, J. O., Mueller, P. J., Orr, K., & Rodriguez, R. 2003, ApJ, 592, 539
- Bellazzini, M., Ferraro, F. R., & Pancino, E. 2001, ApJ, 556, 635

¹⁶We summarize the different coordinate system conventions between astronomical software in Table 14.

¹⁷VARTOOLS is available from Joel Hartman at <https://www.cfa.harvard.edu/~jhartman/vartools/>.

- Bellazzini, M., Ferraro, F. R., Sollima, A., Pancino, E., & Origlia, L. 2004, *A&A*, 424, 199
- Benedict, G. F., et al. 2002, *AJ*, 124, 1695
- Berdnikov, L. N., & Turner, D. G. 1995, *Astronomy Letters*, 21, 717
- . 2001, *ApJS*, 137, 209
- Berdnikov, L. N. 1997, *VizieR Online Data Catalog*, 2217, 0
- Bersier, D. 2001, in *Bulletin of the American Astronomical Society*, Vol. 33, *Bulletin of the American Astronomical Society*, 1518–+
- Bertin, E., & Arnouts, S. 1996, *A&AS*, 117, 393
- Bird, J. C., Stanek, K. Z., & Prieto, J. L. 2009, *ApJ*, 695, 874
- Bonanos, A. Z., & Stanek, K. Z. 2003, *ApJ*, 591, L111
- Bonanos, A. Z., et al. 2006, *ApJ*, 652, 313
- Bono, G., Caputo, F., Fiorentino, G., Marconi, M., & Musella, I. 2008, *ApJ*, 684, 102
- Bresolin, F. 2007, *ApJ*, 656, 186
- Burke, Jr., E. W., Rolland, W. W., & Boy, W. R. 1970, *JRASC*, 64, 353
- Caldwell, J. A. R., & Coulson, I. M. 1986, *MNRAS*, 218, 223
- . 1987, *AJ*, 93, 1090
- Corwin, Jr., H. G., Buta, R. J., & de Vaucouleurs, G. 1994, *AJ*, 108, 2128
- Coulson, I. M., & Caldwell, J. A. R. 1985, *South African Astronomical Observatory Circular*, 9, 5
- de Vaucouleurs, G., de Vaucouleurs, A., Corwin, Jr., H. G., Buta, R. J., Paturel, G., & Fouque, P. 1991, *Third Reference Catalogue of Bright Galaxies (Volume 1-3, XII, 2069 pp. 7 figs.. Springer-Verlag Berlin Heidelberg New York)*
- Dworetzky, M. M. 1983, *MNRAS*, 203, 917
- Eastman, J., Siverd, R., & Gaudi, B. S. 2010, *PASP*, 122, 935
- Feldmeier, J. J., Ciardullo, R., & Jacoby, G. H. 1996, *ApJ*, 461, L25+
- Fiorentino, G., Caputo, F., Marconi, M., & Musella, I. 2002, *ApJ*, 576, 402
- Ford, H. C., et al. 2003, in *SPIE Conference Series*, Vol. 4854, *SPIE Conference Series*, ed. J. C. Blades & O. H. W. Siegmund, 81–94

- Fouqué, P., Storm, J., & Gieren, W. 2003, in *Lecture Notes in Physics*, Berlin Springer Verlag, Vol. 635, *Stellar Candles for the Extragalactic Distance Scale*, ed. D. Alloin & W. Gieren, 21–44
- Freedman, W. L., & Madore, B. F. 1990, *ApJ*, 365, 186
- Freedman, W. L., et al. 1994, *ApJ*, 427, 628
- . 2001, *ApJ*, 553, 47
- Gieren, W. 1981, *ApJS*, 47, 315
- Gould, A. 1994, *ApJ*, 426, 542
- Groenewegen, M. A. T., Romaniello, M., Primas, F., & Mottini, M. 2004, *A&A*, 420, 655
- Hartman, J. D., Gaudi, B. S., Holman, M. J., McLeod, B. A., Stanek, K. Z., Barranco, J. A., Pinsonneault, M. H., & Kalirai, J. S. 2008, *ApJ*, 675, 1254
- Henden, A. A. 1996, *AJ*, 111, 902
- Henderson, C. B., Stanek, K. Z., Pejcha, O., & Prieto, J. L. 2010, arXiv:1009.5673
- Herrnstein, J. R., et al. 1999, *Nature*, 400, 539
- Humphreys, E. M. L., Reid, M. J., Greenhill, L. J., Moran, J. M., & Argon, A. L. 2008, *ApJ*, 672, 800
- Joye, W. A., & Mandel, E. 2003, in *ASP Conference Series*, Vol. 295, *Astronomical Data Analysis Software and Systems XII*, ed. H. E. Payne, R. I. Jedrzejewski, & R. N. Hook, 489–+
- Jurcevic, J. S., Pierce, M. J., & Jacoby, G. H. 2000, *MNRAS*, 313, 868
- Kelson, D. D., et al. 1996, *ApJ*, 463, 26
- Kennicutt, Jr., R. C. 1998, *ApJ*, 498, 541
- Kennicutt, Jr., R. C., Bresolin, F., & Garnett, D. R. 2003, *ApJ*, 591, 801
- Kennicutt, Jr., R. C., & Garnett, D. R. 1996, *ApJ*, 456, 504
- Kennicutt, Jr., R. C., et al. 1998, *ApJ*, 498, 181
- Khan, R., Stanek, K. Z., Prieto, J. L., Kochanek, C. S., Thompson, T. A., & Beacom, J. F. 2010, *ApJ*, 715, 1094
- Kochanek, C. S. 1997, *ApJ*, 491, 13
- Kozłowski, S., et al. 2010, *ApJ*, 716, 530
- Landolt, A. U. 1992, *AJ*, 104, 340

- Lee, M. G., Freedman, W. L., & Madore, B. F. 1993, *ApJ*, 417, 553
- Macri, L. M., Stanek, K. Z., Bersier, D., Greenhill, L. J., & Reid, M. J. 2006, *ApJ*, 652, 1133
- Macri, L. M., et al. 2001, *ApJ*, 549, 721
- Madore, B. F. 1982, *ApJ*, 253, 575
- Madore, B. F., & Freedman, W. L. 2005, *ApJ*, 630, 1054
- Madore, B. F., Mager, V., & Freedman, W. L. 2009, *ApJ*, 690, 389
- Mager, V. A., Madore, B. F., & Freedman, W. L. 2008, *ApJ*, 689, 721
- Markwardt, C. B. 2009, in *Astronomical Society of the Pacific Conference Series*, Vol. 411, *Astronomical Society of the Pacific Conference Series*, ed. D. A. Bohlender, D. Durand, & P. Dowler, 251–+
- Méndez, B., Davis, M., Moustakas, J., Newman, J., Madore, B. F., & Freedman, W. L. 2002, *AJ*, 124, 213
- Mochejska, B. J., Macri, L. M., Sasselov, D. D., & Stanek, K. Z. 2000, *AJ*, 120, 810
- Moffett, T. J., & Barnes, III, T. G. 1984, *ApJS*, 55, 389
- Moffett, T. J., Gieren, W. P., Barnes, III, T. G., & Gomez, M. 1998, *ApJS*, 117, 135
- Nataf, D. M., Stanek, K. Z., & Bakos, G. Á. 2010, *Acta Astron.*, 60, 261
- Ochsenbein, F., Bauer, P., & Marcout, J. 2000, *A&AS*, 143, 23
- Pavlovsky, C., et al. 2005, *The ACS Data Handbook, Version 4.0* (Baltimore:STScI)
- Peeples, M. S., Stanek, K. Z., & DePoy, D. L. 2007, *Acta Astronomica*, 57, 173
- Riess, A. G., et al. 2009a, *ApJ*, 699, 539
- . 2009b, *ApJS*, 183, 109
- Rizzi, L., Tully, R. B., Makarov, D., Makarova, L., Dolphin, A. E., Sakai, S., & Shaya, E. J. 2007, *ApJ*, 661, 815
- Saha, A., Sandage, A., Tammann, G. A., Dolphin, A. E., Christensen, J., Panagia, N., & Macchetto, F. D. 2001, *ApJ*, 562, 314
- Saha, A., Thim, F., Tammann, G. A., Reindl, B., & Sandage, A. 2006, *ApJS*, 165, 108
- Sakai, S., Ferrarese, L., Kennicutt, Jr., R. C., & Saha, A. 2004, *ApJ*, 608, 42
- Sakai, S., Madore, B. F., & Freedman, W. L. 1996, *ApJ*, 461, 713

- Salaris, M., Cassisi, S., & Weiss, A. 2002, *PASP*, 114, 375
- Sandage, A., & Tammann, G. A. 1981, in *Carnegie Inst. of Washington, Publ. 635; Vol. 0; Page 0*, 0–+
- Sandage, A., & Tammann, G. A. 2008, *ApJ*, 686, 779
- Sandage, A., Tammann, G. A., & Reindl, B. 2004, *A&A*, 424, 43
- Sandage, A., Tammann, G. A., Saha, A., Reindl, B., Macchetto, F. D., & Panagia, N. 2006, *ApJ*, 653, 843
- Sasselov, D. D., et al. 1997, *A&A*, 324, 471
- Schlegel, D. J., Finkbeiner, D. P., & Davis, M. 1998, *ApJ*, 500, 525
- Sebo, K. M., et al. 2002, *VizieR Online Data Catalog*, 214, 20071
- Sirianni, M., et al. 2005, *PASP*, 117, 1049
- Stanek, K. Z., & Udalski, A. 1999, *arXiv:astro-ph/9909346*
- Stetson, P. B. 1987, *PASP*, 99, 191
- . 1992, *JRASC*, 86, 71
- . 1994, *PASP*, 106, 250
- . 1996, *PASP*, 108, 851
- Stetson, P. B., et al. 1998, *ApJ*, 508, 491
- Stift, M. J. 1990, *A&A*, 229, 143
- . 1995, *A&A*, 301, 776
- Stothers, R. B. 1988, *ApJ*, 329, 712
- Szczygieł, D. M., Stanek, K. Z., Bonanos, A. Z., Pojmański, G., Pilecki, B., & Prieto, J. L. 2010, *AJ*, 140, 14
- Tammann, G. A., Sandage, A., & Reindl, B. 2003, *A&A*, 404, 423
- Udalski, A., Soszynski, I., Szymanski, M., Kubiak, M., Pietrzynski, G., Wozniak, P., & Zebrun, K. 1999a, *Acta Astron.*, 49, 223
- . 1999b, *Acta Astron.*, 49, 437
- Valle, G., Marconi, M., Degl’Innocenti, S., & Prada Moroni, P. G. 2009, *A&A*, 507, 1541

Welch, D. L., & Stetson, P. B. 1993, *AJ*, 105, 1813

Wozniak, P. R. 2000, *Acta Astron.*, 50, 421

Yoachim, P., McCommas, L. P., Dalcanton, J. J., & Williams, B. F. 2009, *AJ*, 137, 4697

Zaritsky, D., Hill, J. M., & Elston, R. 1990, *AJ*, 99, 1108

This preprint was prepared with the AAS L^AT_EX macros v5.2.

Table 1. Log of Observations

Visit Number	UT Date	(BJD _{TDB} – 2,450,000.0) ^a at Mid-exposure			
		I	V	I	V
F1-01	2006 Dec 23	4092.03116	4092.03899	4092.04805	4092.05619
F1-02	2006 Dec 24	4093.16580	4093.17363	4093.18269	4093.19083
F1-03	2006 Dec 25	4094.62862	4094.63644	4094.64551	4094.65364
F1-04	2006 Dec 26	4095.89387	4095.90169	4095.91076	4095.91889
F1-05	2006 Dec 28	4097.75827	4097.76609	4097.77515	4097.78329
F1-06	2006 Dec 30	4099.88941	4099.89724	4099.90630	4099.91444
F1-07	2007 Jan 01	4101.75398	4101.76181	4101.77087	4101.77901
F1-08	2007 Jan 04	4104.48410	4104.49193	4104.50099	4104.50913
F1-09	2007 Jan 07	4107.74682	4107.75464	4107.76370	4107.77184
F1-10	2007 Jan 11	4111.94164	4111.94947	4111.95853	4111.96666
F1-11	2007 Jan 17	4117.40136	4117.40919	4117.41825	4117.42639
F1-12	2007 Jan 21	4121.72890	4121.73673	4121.74579	4121.75393
F2-01	2006 Dec 25	4094.69519	4094.70301	4094.71207	4094.72021
F2-02	2006 Dec 26	4095.82724	4095.83507	4095.84413	4095.85227
F2-03	2006 Dec 28	4097.02585	4097.03367	4097.04273	4097.05087
F2-04	2006 Dec 30	4099.02364	4099.03147	4099.04053	4099.04867
F2-05	2006 Dec 31	4100.88828	4100.89611	4100.90517	4100.91331
F2-06	2007 Jan 01	4101.82055	4101.82837	4101.83744	4101.84557
F2-07	2007 Jan 05	4105.09577	4105.10359	4105.15438	4105.16252
F2-08	2007 Jan 07	4107.16210	4107.16993	4107.21903	4107.22716
F2-09	2007 Jan 10	4110.22705	4110.23487	4110.27747	4110.28560
F2-10	2007 Jan 14	4114.82183	4114.82965	4114.87171	4114.87985
F2-11	2007 Jan 18	4118.61321	4118.62103	4118.66682	4118.67496
F2-12	2007 Jan 23	4123.79267	4123.80049	4123.80955	4123.81769

Note. — Table discussed in §2.

^a See Eastman et al. (2010) for details.

Table 2. Secondary Standards

ID	R.A. (J2000)	Dec. (J2000)	X pixels	Y pixels	Magnitudes		
					V	I	I _V
F1-71	210.86852031	54.35418692	2544.1	2268.0	21.393(005)	20.532(005)	–0.2
F1-58	210.85461416	54.39176894	281.2	3861.6	21.333(005)	20.721(005)	–0.4
F1-162	210.89357513	54.36263801	1573.1	1538.3	22.011(007)	20.872(006)	–0.3
F1-208	210.84008842	54.35383418	3033.3	3356.5	22.016(007)	20.892(006)	–0.5
F1-137	210.82119974	54.34762558	3754.2	3911.8	21.821(006)	21.154(007)	–0.8
F1-151	210.85330380	54.34252050	3566.6	2527.9	21.856(006)	21.201(007)	0.9
F1-103	210.88537412	54.37791726	695.1	2284.8	21.649(005)	21.735(009)	0.4
F1-185	210.85991217	54.36690151	1842.5	2958.0	21.931(006)	21.226(007)	0.9
F1-601	210.90181610	54.35600312	1877.6	1033.3	22.701(006)	20.896(006)	0.8
F1-181	210.87887687	54.37002640	1324.4	2313.8	21.992(006)	21.477(008)	–0.4

Table to be published in its entirety in machine-readable form.

Note. — R.A. and Dec. are in units of degrees. Errors in mean magnitudes and semiamplitudes are in units of 0.001 mag. Table discussed in §3.2.

Table 3. Cepheid Variables

ID	Period (days)	R.A. (J2000)	Dec. (J2000)	X pixels	Y pixels	Magnitudes		Amp.		I_V
						V	I	V	I	
F1-567	40.9345(1.0315)	210.87019095	54.34667242	3014.6	1992.2	22.985(008)	22.171(006)	0.158	0.091	75.3
F1-773	75.3739(2.2386)	210.89765450	54.37240300	859.1	1655.8	22.676(016)	21.754(017)	0.315	0.206	287.1
F1-1274	49.4143(2.3786)	210.84511130	54.35727011	2723.2	3258.9	23.290(019)	22.413(009)	0.505	0.261	342.5
F1-1552	42.6833(3.6532)	210.85128425	54.38254091	947.1	3730.9	23.412(044)	22.512(026)	0.519	0.310	306.6
F1-1619	30.8813(0.7128)	210.88234973	54.36916648	1324.6	2155.5	23.532(014)	22.700(014)	0.503	0.345	668.9
F1-1721	27.2601(0.4105)	210.86452566	54.35514022	2546.3	2449.2	23.626(016)	22.849(014)	0.477	0.278	275.8
F1-1767	21.7926(0.3649)	210.86424080	54.34258320	3383.2	2107.0	23.669(021)	22.922(024)	0.335	0.202	129.5
F1-1890	30.4055(0.7575)	210.83646784	54.36458112	2380.2	3798.2	23.699(015)	22.755(013)	0.479	0.269	501.1
F1-1975	30.4193(0.5237)	210.86646959	54.34309782	3312.5	2035.4	23.728(016)	22.797(012)	0.501	0.266	241.0
F1-2045	22.8373(0.1005)	210.87188971	54.34614160	3021.9	1911.6	23.776(013)	23.083(015)	0.446	0.302	236.3

Table to be published in its entirety in machine-readable form.

Note. — R.A. and Dec. are in units of degrees. Astrometry presented is referenced to the HST headers of j9o401010_drz.fits for Field 1 and j9o413010_drz.fits for Field 2. Errors in mean magnitudes and semiamplitudes are in units of 0.001 mag. Table discussed in §4.2.

Table 4. Rejected Cepheid Candidates

ID	Period (days)	R.A. (J2000)	Dec. (J2000)	X pixels	Y pixels	Magnitudes		Amp.		I_V	<i>Reason</i> ^a
						V	I	V	I		
F1-381	146.449	210.86070136	54.35415151	2674.5	2569.1	22.525(007)	22.265(011)	0.136	0.140	98.5	A
F1-757	166.814	210.84322037	54.38390199	988.9	4080.5	22.968(010)	22.648(014)	0.281	0.226	62.6	A
F1-1005	76.313	210.87279394	54.36153133	1987.2	2309.6	22.883(015)	21.845(010)	0.336	0.260	422.4	A
F1-1357	5.986	210.86954527	54.33204480	3994.6	1605.6	23.518(009)	23.128(014)	0.120	0.174	40.6	A
F1-1378	168.978	210.88086502	54.33618592	3534.5	1284.7	22.867(057)	22.828(070)	1.279	0.295	19.2	A
F1-1576	148.915	210.88486096	54.35099847	2487.3	1547.2	23.457(008)	23.252(016)	0.139	0.145	21.0	A
F1-2754	13.727	210.88137081	54.37066234	1241.5	2235.4	24.022(013)	23.661(019)	0.249	0.212	62.8	A
F1-2812	34.901	210.86097991	54.37769971	1109.2	3220.5	23.966(013)	22.849(009)	0.314	0.278	135.8	A
F1-2883	36.574	210.87213007	54.36013865	2090.4	2296.1	23.930(011)	23.003(012)	0.374	0.303	236.1	A
F1-4020	19.565	210.85013743	54.37919292	1187.8	3681.1	24.339(016)	23.475(017)	0.190	0.152	25.2	A

Table to be published in its entirety in machine-readable form.

Note. — R.A. and Dec. are in units of degrees. Astrometry presented is referenced to the HST headers of j9o401010_drz.fits for Field 1 and j9o413010_drz.fits for Field 2. Errors in mean magnitudes are in units of 0.001 mag. Table discussed in §4.2.

^a Reasons for the Cepheid candidates rejection; **A**: Amplitude ratio ratio cut. **B**: Blue blends. **C**: Large Extinction. **D**: Population II Cepheids. **E**: Candidates removed by period cut. **F**: Candidates removed by iterative sigma clipping.

Table 5. Sample Selection

Sample Cuts	Field	
	F1	F2
Initial Cepheid Candidates	632	595
1. Amplitude Ratio	–139	–121
2. $E(V - I) < (2\sigma \text{ foreground})$	–29	–19
3. $E(V - I) > 0.5 \text{ mag}$	–24	–11
4. $\Delta\mu_0 > 11.5 \text{ mag}$	–6	–7
5. Period $< 3 \text{ days}$	–2	–4
6. σ clipping	–21	–17
Final Sample	411	416

Note. — Effects of sample selection described in §4.4.

Table 6. Cepheid Variables: Calculated Quantities

ID	Period (days)	F-Test χ^2 ratio	$\Delta\mu_{\text{LMC}}$ (mag)	$E(V - I)$ (mag)	$E(B - V)$ (mag)	ρ/ρ_{iso}	$12 + \log(\text{O}/\text{H})$ (dex)
F1-567	40.934	19.381	10.350(074)	0.020(020)	0.015(014)	0.1696	8.60
F1-773	75.374	28.559	10.644(099)	0.075(074)	0.054(054)	0.2551	8.52
F1-1274	49.414	82.090	10.769(101)	0.066(065)	0.048(047)	0.1131	8.65
F1-1552	42.683	35.455	10.626(164)	0.102(102)	0.074(074)	0.1897	8.58
F1-1619	30.881	59.668	10.453(077)	0.062(062)	0.045(045)	0.2160	8.56
F1-1721	27.260	44.162	10.507(072)	0.017(017)	0.013(012)	0.1573	8.61
F1-1767	21.793	28.944	10.303(088)	0.008(007)	0.006(005)	0.1569	8.61
F1-1890	30.405	44.678	10.324(077)	0.175(175)	0.128(127)	0.1097	8.65
F1-1975	30.419	45.180	10.384(072)	0.163(163)	0.119(118)	0.1620	8.60
F1-2045	22.837	38.497	10.610(068)	–0.051(163)	–0.037(118)	0.1740	8.59

Table to be published in its entirety in machine-readable form.

Note. — Errors in the mean colors and the LMC relative distance moduli are in units of 0.001 mag. Table discussed in §4.2.

Table 7. Error Budget of the Cepheid Distance Scale

Error source	LMC relative μ_0	This Work M101 μ_0	Goal ^a M101 μ_0
A. Fiducial galaxy	...	NGC 4258	NGC 4258
S1a. Distance modulus (sys)	0.12	...
S1b. Distance modulus (ran)	0.09	...
S1. Distance modulus (tot)	0.15	0.07
B. Photometric calibration			
S2a. V zeropoint	0.02	0.02	...
S2b. I zeropoint	0.02	0.02	...
S2. Photometry (sys)	0.05	0.05	...
S3. NGC 4258 ^b Photometry (sys)	0.05	...
R1. Photometry (ran)	0.03	0.03	0.03
R2. NGC 4258 ^b Photometry (ran)	0.03	0.03
C. Extinction corrections			
R3. Uncertainty in R_V	0.02	0.02	0.02
R4. NGC 4258 ^b Uncertainty in R_V	0.02	0.02
D. Corrections to LMC Metallicity			
S4. Adopted correction	0.04	0.04	0.04
S5. NGC 4258 ^b Adopted correction	0.04	0.04
R5. Zero-point	0.02	0.02	0.02
R6. NGC 4258 ^b Zero-point	0.02
R_T . Total random	0.04	0.05	0.06
S_T . Total systematic	0.07	0.18	0.09
Combined error (mag)	0.08	0.18	0.11
Combined error (%)	4	8	5

Note. — All errors expressed in magnitudes unless otherwise indicated. Table discussed in §5.3 and §9.

^a Goal errors are calculated using the anticipated improvement in the maser distance determination to NGC 4258 (Humphreys et al. 2008).

^b This work uses the Macri et al. (2006) Cepheid NGC 4258 distance. Goal work errors are based on using the same analysis in this paper on the Macri et al. (2006) HST/ACS Cepheid observations.

Table 8. Recent Distance Determinations to M101

Study	Method ^a	LMC μ_0 mag	M101 μ_0 mag	LMC-relative $\Delta\mu_0^b$ mag	Outer/Inner Field
This work	Cepheids	$18.41 \pm 0.10_r \pm 0.13_s$	$29.04 \pm 0.05_r \pm 0.18_s$	$10.63 \pm 0.02_r \pm 0.04_s$	inner
This work	TRGB	...	$29.05 \pm 0.06_r \pm 0.12_s$...	inner
Saha et al. (2006)	Cepheids	18.54 ^c	29.16 ± 0.04	10.62 ± 0.04	inner
Saha et al. (2006)	Cepheids	18.54 ^c	29.18 ± 0.08	10.64 ± 0.08	outer
Freedman et al. (2001)	Cepheids	18.50	29.13 ± 0.11	10.63 ± 0.11	outer
Macri et al. (2001)	Cepheids	18.50	29.19 ± 0.08	10.69 ± 0.08	inner
Macri et al. (2001)	Cepheids	18.50	29.53 ± 0.03	11.03 ± 0.03	outer
Stetson et al. (1998)	Cepheids	18.50	29.21 ± 0.17	10.71 ± 0.17	inner
Kennicutt et al. (1998)	Cepheids	18.50	29.21 ± 0.09	10.71 ± 0.09	inner
Kennicutt et al. (1998)	Cepheids	18.50	29.34 ± 0.08	10.84 ± 0.08	outer
Kelson et al. (1996)	Cepheids	18.50	29.34 ± 0.17	10.84 ± 0.17	outer
Rizzi et al. (2007)	TRGB	...	29.34 ± 0.09
Sakai et al. (2004)	TRGB	...	29.42 ± 0.02
Jurcevic et al. (2000)	RSV	18.50 ± 0.10	29.40 ± 0.16	10.90 ± 0.16	...
Feldmeier et al. (1996)	PNLF	...	29.42 ± 0.15

Note. — Table discussed in §5.3, §7 and §9.

^a TRGB: tip of the red giant branch; RSV:red supergiant variable stars; PNLF: planetary nebula luminosity function.

^b We simply subtract each measurements adopted LMC Distance Modulus from the M101 Distance Modulus to obtain the LMC-relative Distance Modulus for rough comparisons with our measurements.

^c Zero point also assumes a distance modulus to Pleiads is 5.61 mag and relays on the Baade-Becker-Wesselink distances to 32 Cepheids in Fouqué et al. (2003) and Barnes et al. (2003).

Table 9. Model Wesenheit P-L Fit Parameters

Model	a_w^S mag $\log(\text{day})^{-1}$	a_w^I mag $\log(\text{day})^{-1}$	b_w^S mag	b_w^I mag	χ^2	DoF
Model 1	...	$-3.1^{+0.1}_{-0.1}$...	$22.21^{+0.01}_{-0.01}$	278.8	279
Model 2	...	$-3.1^{+0.1}_{-0.1}$	$0.68^{+0.20}_{-0.18}$	$22.22^{+0.01}_{-0.01}$	263.4	278
Model 3	$-3.4^{+1.5}_{-1.6}$	$-3.1^{+0.1}_{-0.1}$...	$22.20^{+0.01}_{-0.01}$	273.8	278
Model 4	$-2.8^{+1.6}_{-1.6}$	$-3.1^{+0.1}_{-0.1}$	$0.65^{+0.20}_{-0.18}$	$22.21^{+0.01}_{-0.01}$	260.1	277
Restricted Model 1	...	$-3.0^{+0.1}_{-0.1}$...	$22.20^{+0.01}_{-0.01}$	265.0	265
Restricted Model 2	...	$-3.0^{+0.1}_{-0.1}$	$0.68^{+0.20}_{-0.19}$	$22.21^{+0.01}_{-0.01}$	251.3	264
Restricted Model 3	$-3.5^{+1.6}_{-1.7}$	$-3.1^{+0.1}_{-0.1}$...	$22.20^{+0.01}_{-0.01}$	260.7	264
Restricted Model 4	$-2.8^{+1.7}_{-1.7}$	$-3.0^{+0.1}_{-0.1}$	$0.65^{+0.20}_{-0.17}$	$22.21^{+0.01}_{-0.01}$	248.8	263

Note. —

Restricted Models have a 40.0 day maximum period cut imposed. 68% uncertainties and confidence intervals are presented. Table discussed in §6 and §9.

Model 1: constant slope and intercept

Model 2: linearly varying intercept with a constant slope

Model 3: linearly varying slope with a constant intercept

Model 4: linearly varying slope and intercept

Table 10. Model Wesenheit P-L Fit Parameters as a function of [O/H]

Model	a_w^S mag log (day) ⁻¹ dex ⁻¹	a_w^I mag log (day) ⁻¹	b_w^S mag dex ⁻¹	b_w^I mag
Model 1	...	$-3.1^{+0.1}_{-0.1}$...	$22.21^{+0.01}_{-0.01}$
Model 2	...	$-3.1^{+0.1}_{-0.1}$	$-0.75^{+0.21}_{-0.22} \pm 0.06_s$	$22.22^{+0.01}_{-0.01} \pm 0.04_s$
Model 3	$3.8^{+1.7}_{-1.7} \pm 0.3_s$	$-3.1^{+0.1}_{-0.1} \pm 0.2_s$...	$22.20^{+0.01}_{-0.01}$
Model 4	$3.1^{+1.8}_{-1.7} \pm 0.2_s$	$-3.1^{+0.1}_{-0.1} \pm 0.2_s$	$-0.72^{+0.20}_{-0.22} \pm 0.06_s$	$22.21^{+0.01}_{-0.01} \pm 0.04_s$
Restricted Model 1	...	$-3.0^{+0.1}_{-0.1}$...	$22.20^{+0.01}_{-0.01}$
Restricted Model 2	...	$-3.0^{+0.1}_{-0.1}$	$-0.76^{+0.21}_{-0.22} \pm 0.06_s$	$22.21^{+0.01}_{-0.01} \pm 0.04_s$
Restricted Model 3	$3.9^{+1.9}_{-1.8} \pm 0.3_s$	$-3.1^{+0.1}_{-0.1} \pm 0.2_s$...	$22.20^{+0.01}_{-0.01}$
Restricted Model 4	$3.1^{+1.9}_{-1.9} \pm 0.2_s$	$-3.0^{+0.1}_{-0.1} \pm 0.2_s$	$-0.72^{+0.19}_{-0.22} \pm 0.06_s$	$22.21^{+0.01}_{-0.01} \pm 0.04_s$

Note. — Same as Table 9 but model fits are now a function of metallicity using Eq.9. 68% uncertainties and confidence intervals are presented. Table discussed in §6 and §9.

Table 11. Model Wesenheit P-L Comparison

Models Compared	Full Sample		Restricted Sample			
	F-Test	Confidence	$\Delta\chi^2$	F-Test	Confidence	$\Delta\chi^2$
Model 2 vs. Model 1		99.99%	15.5	99.98%		13.7
Model 4 vs. Model 2		93.6%	3.2	89.4%		2.5

Note. — Restricted Sample has a 40.0 day maximum period cut imposed. Table discussed in §6 and §9.

Table 12. Other Objects

ID	R.A.	Dec.	X	Y	Magnitudes		ρ/ρ_{iso}	12 + log(O/H) (dex)
	(J2000)	(J2000)	pixels	pixels	V	I		
F1-13	210.86366905	54.35792401	2375.8	2560.5	20.763	20.145	0.1577	8.61
F1-29	210.84194069	54.34349859	3688.0	2994.3	21.116	20.243	0.1012	8.66
F1-113	210.88622020	54.37159190	1100.4	2074.4	21.601	20.522	0.2286	8.54
F1-54	210.83356976	54.33960030	4083.5	3208.2	21.381	20.970	0.0868	8.67
F1-258	210.85598559	54.37583152	1314.9	3360.8	22.239	21.909	0.1771	8.59
F1-347	210.81751077	54.34294154	4125.0	3922.7	22.660	22.840	0.0450	8.71
F2-24	210.75884312	54.34062464	1344.9	595.3	20.549	19.616	0.1160	8.65
F2-91	210.76574754	54.35390318	350.0	685.4	21.265	20.443	0.0919	8.67
F2-37	210.70780831	54.32347179	3292.9	2118.5	20.917	20.519	0.2704	8.51
F2-48	210.69712403	54.35234385	1533.4	3312.8	21.029	21.079	0.2601	8.52
F2-660	210.70992763	54.34032812	2134.3	2490.6	22.718	21.845	0.2367	8.54
F2-367	210.70670420	54.34630827	1785.8	2777.3	22.297	22.200	0.2392	8.53

Note. — R.A. and Dec. are in units of degrees. Astrometry presented is referenced to the HST headers of j9o401010_drz.fits for Field 1 and j9o413010_drz.fits for Field 2. Table discussed in §8.

Table 13. Other Possible Periodic Objects

ID	Period (days)	R.A. (J2000)	Dec (J2000)	X pixels	Y pixels	Magnitudes		ρ/ρ_{iso}	12 + log (O/H) (dex)
						V	I		
F1-574	0.508	210.82228318	54.34545471	3880.3	3808.9	22.806	22.747	0.0516	8.70
F2-271	10.779	210.75024732	54.35297493	656.0	1263.2	21.998	21.962	0.1291	8.63

Note. — R.A. and Dec. are in units of degrees. Astrometry presented is referenced to the HST headers of j9o401010_drz.fits for Field 1 and j9o413010_drz.fits for Field 2. Table discussed in §8.

Table 14. Pixel Coordinate Conventions

Software	Coordinate of Center of Lower Left Pixel	
	x pixel	y pixel
DOLPHOT	0.5	0.5
IRAF	1.0	1.0
DAOPHOT	1.0	1.0
ISIS	0.0	0.0
DS9 ^a	1.0	1.0

Note. — Table discussed in §A.

^a Joye & Mandel (2003)

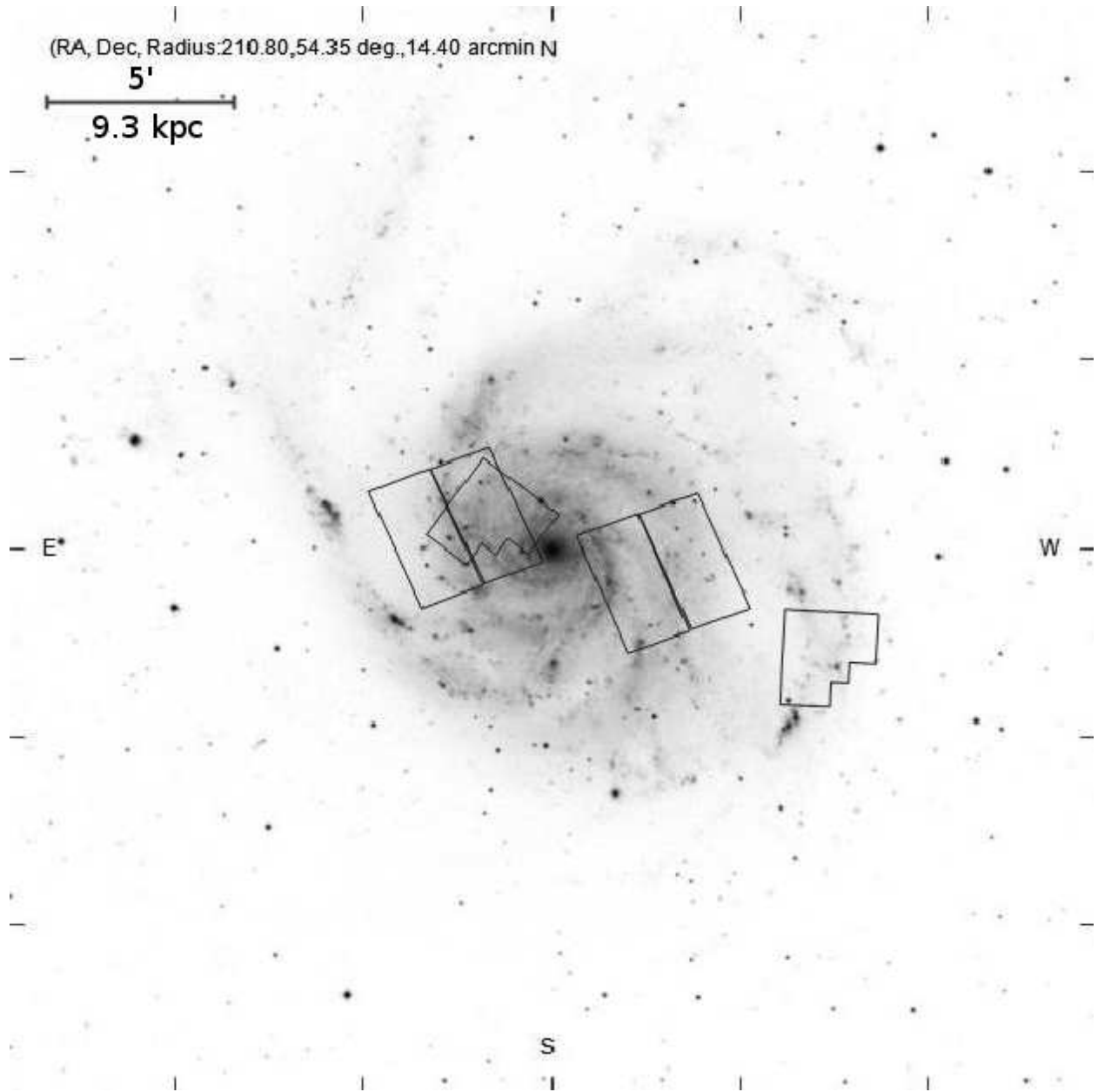


Fig. 1.— SDSS image of M101 showing the two fields observed with ACS/WFC (rectangular shape) which are used in this study and the two fields observed with WFPC2 ('stealth fighter' shape) for the Hubble Key Project. For both projects, Field 1 is in the East and Field 2 is in the West. Figure discussed in §2.



Fig. 2.— HST ACS/WFC F555W and F814W 2-band color composite image of the ISIS reference images for Field 1 in M101. The absolute orientation of the field is shown in Fig. 1. The ACS/WFC field of view is $202''$ on each side, corresponding to a physical size of 6.3 kpc. Figure discussed in §3.1.



Fig. 3.— HST ACS/WFC F555W and F814W 2-band color composite image of the ISIS reference images for Field 2 in M101. The absolute orientation of the field is shown in Fig. 1. The ACS/WFC field of view is $202''$ on each side, corresponding to a physical size of 6.3 kpc. Figure discussed in §3.1.

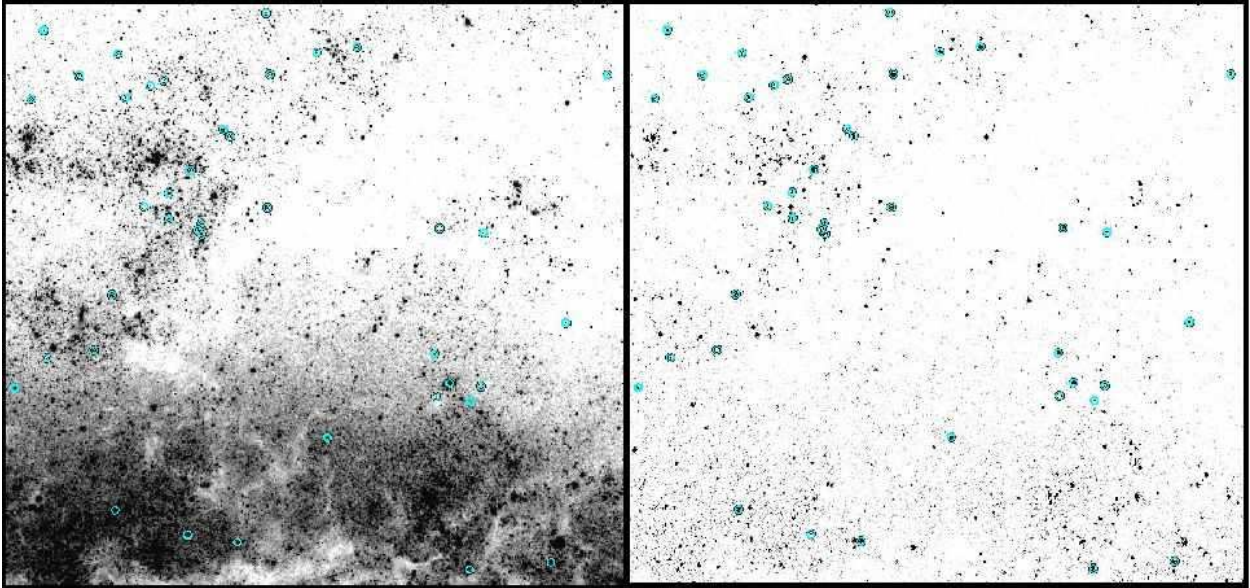


Fig. 4.— Inner region of Field 2 in M101 from our F555W ISIS reference image (left) and our F555W ISIS variability map (right). Cepheids from the final sample found in §4 are marked by teal annuli. The region is $\approx 62''$ on each side, corresponding to a physical size of ≈ 1.9 kpc. Figure discussed in §3.1.

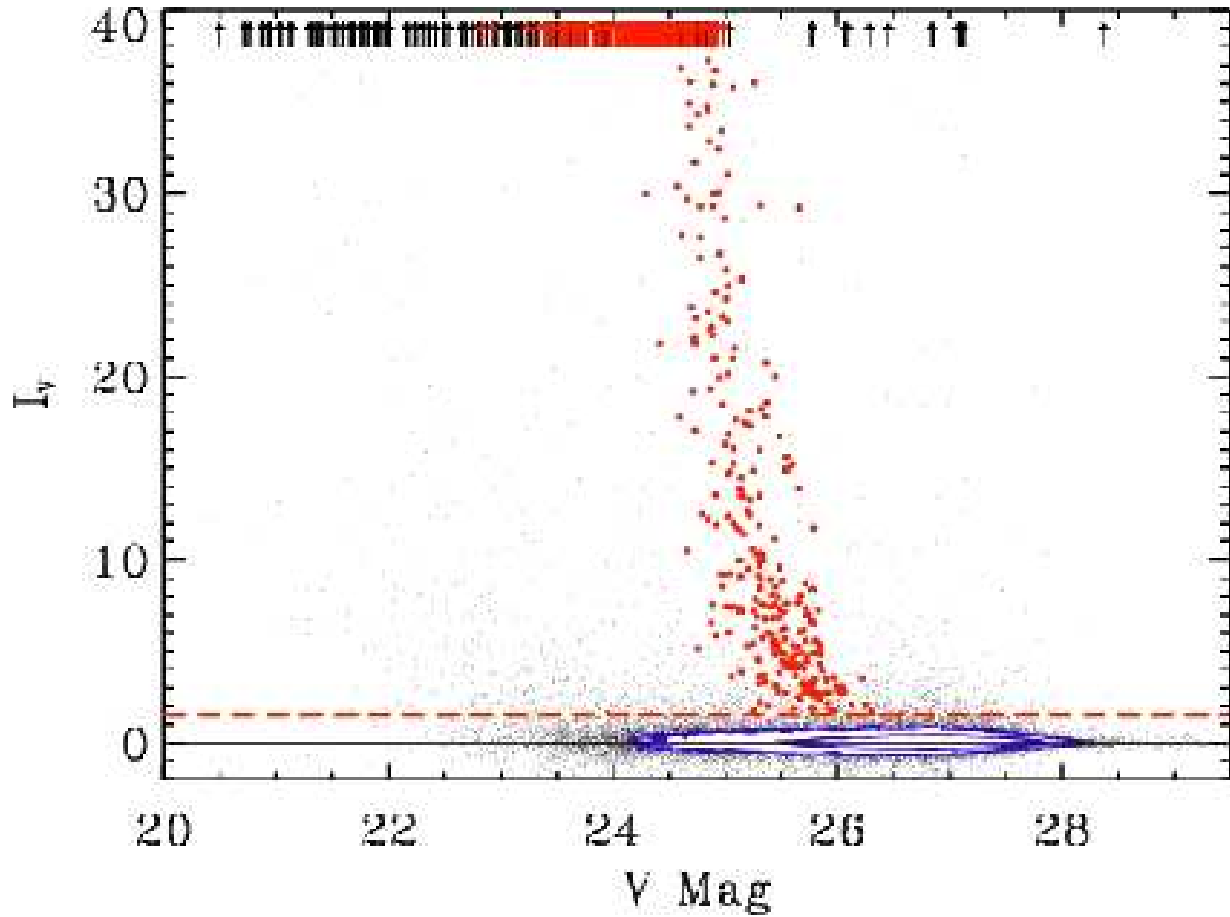


Fig. 5.— Welch-Stetson variability index I_V (Welch & Stetson 1993) versus V -band magnitude for the objects in Field 1. The black solid line marks a variability index of 0. The red dashed line marks the $I_V \geq 1.5$ criteria used to select variables. Objects with a $I_V > 40$ are marked with arrows. The blue lines represent the 68% and 90% contours. Red circles and red arrows mark the locations of the final Cepheid sample found in §4. Figure discussed in §4.1.

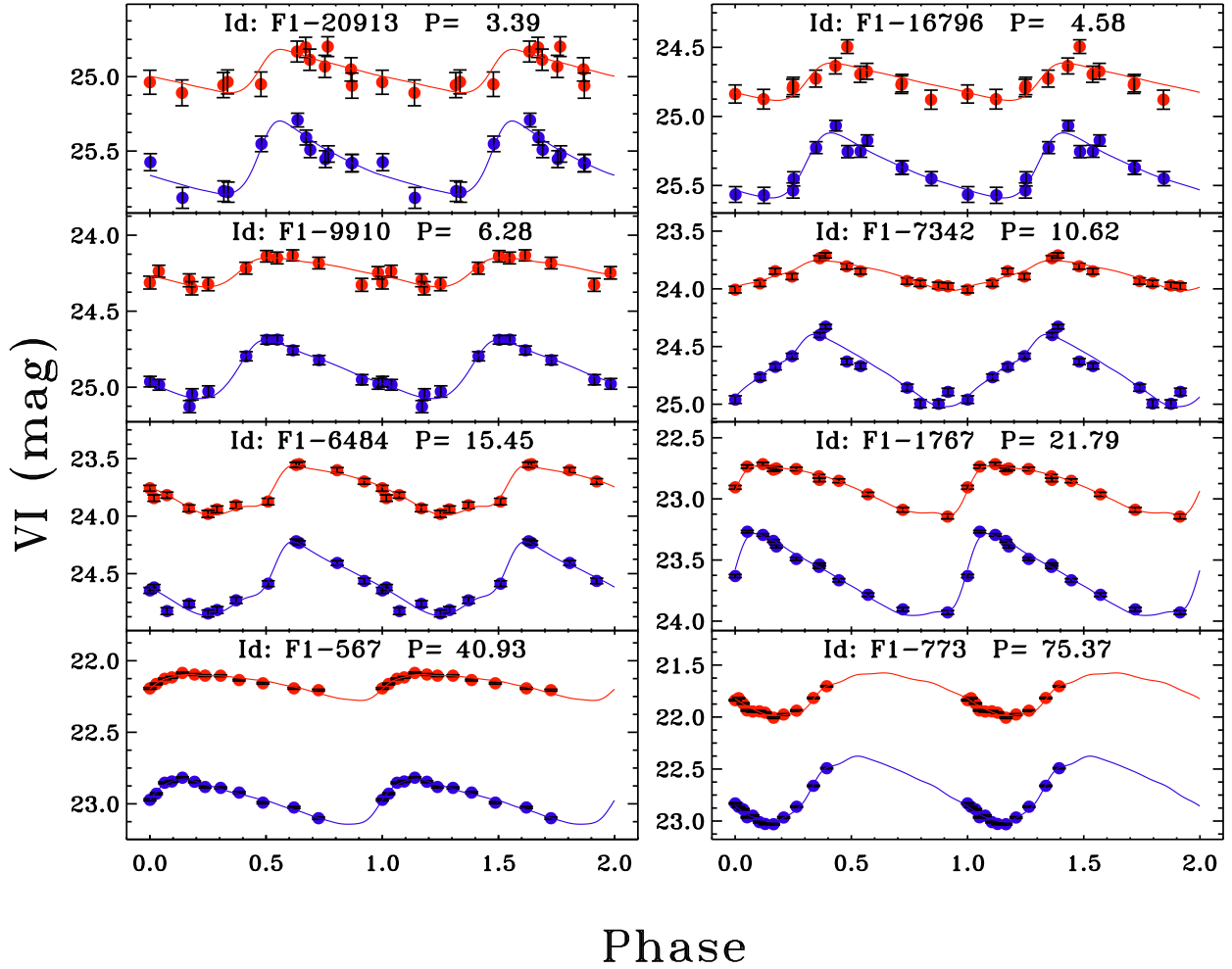


Fig. 6.— Cepheid light curves of various periods from Field 1. Blue (bottom): V filter light curves. Red (top): I filter light curves. Solid line shows the best-fit light curve template from Yoachim et al. (2009) with additional fit amplitude parameters. Figure discussed in §4.2.

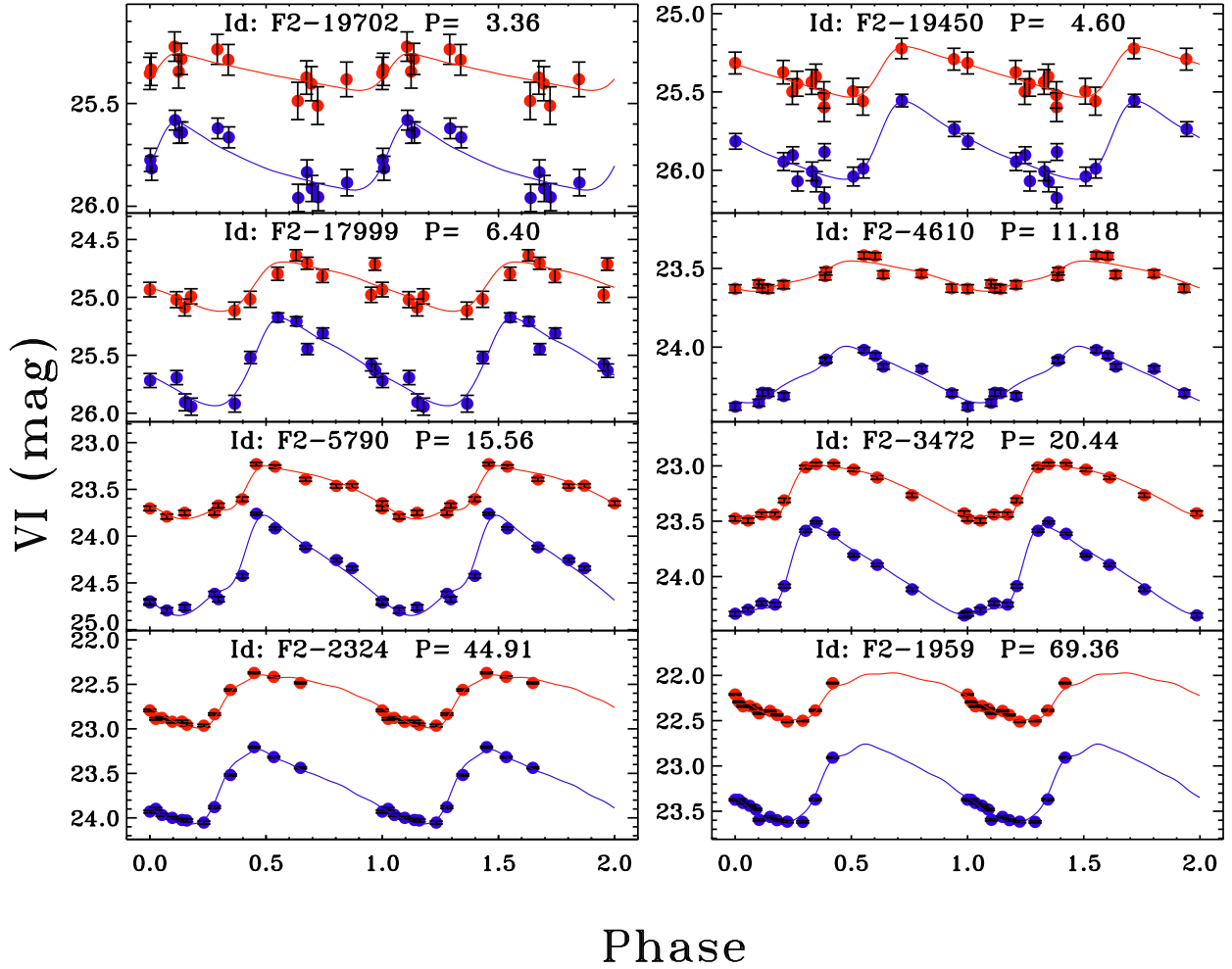


Fig. 7.— Cepheid light curves of various periods from Field 2. Blue (bottom): V filter light curves. Red (top): I filter light curves. Solid line shows the best-fit light curve template from Yoachim et al. (2009) with additional fit amplitude parameters. Figure discussed in §4.2.

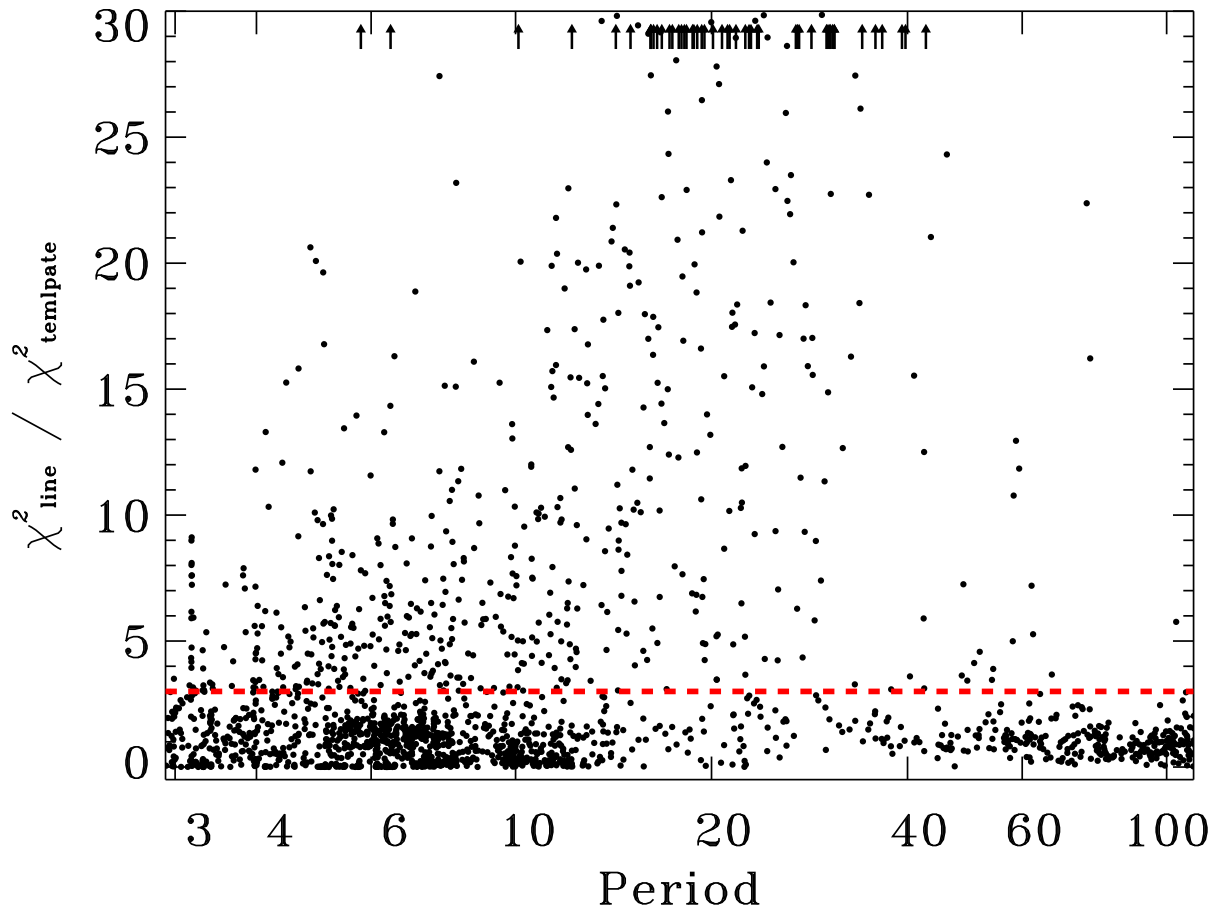


Fig. 8.— Distribution of $\Delta\chi^2/\text{dof}$ as a function of the template model period for objects in Field 1. Objects with $\Delta\chi^2/\text{dof} > 30$ are represented by arrows. Figure discussed in §4.2.

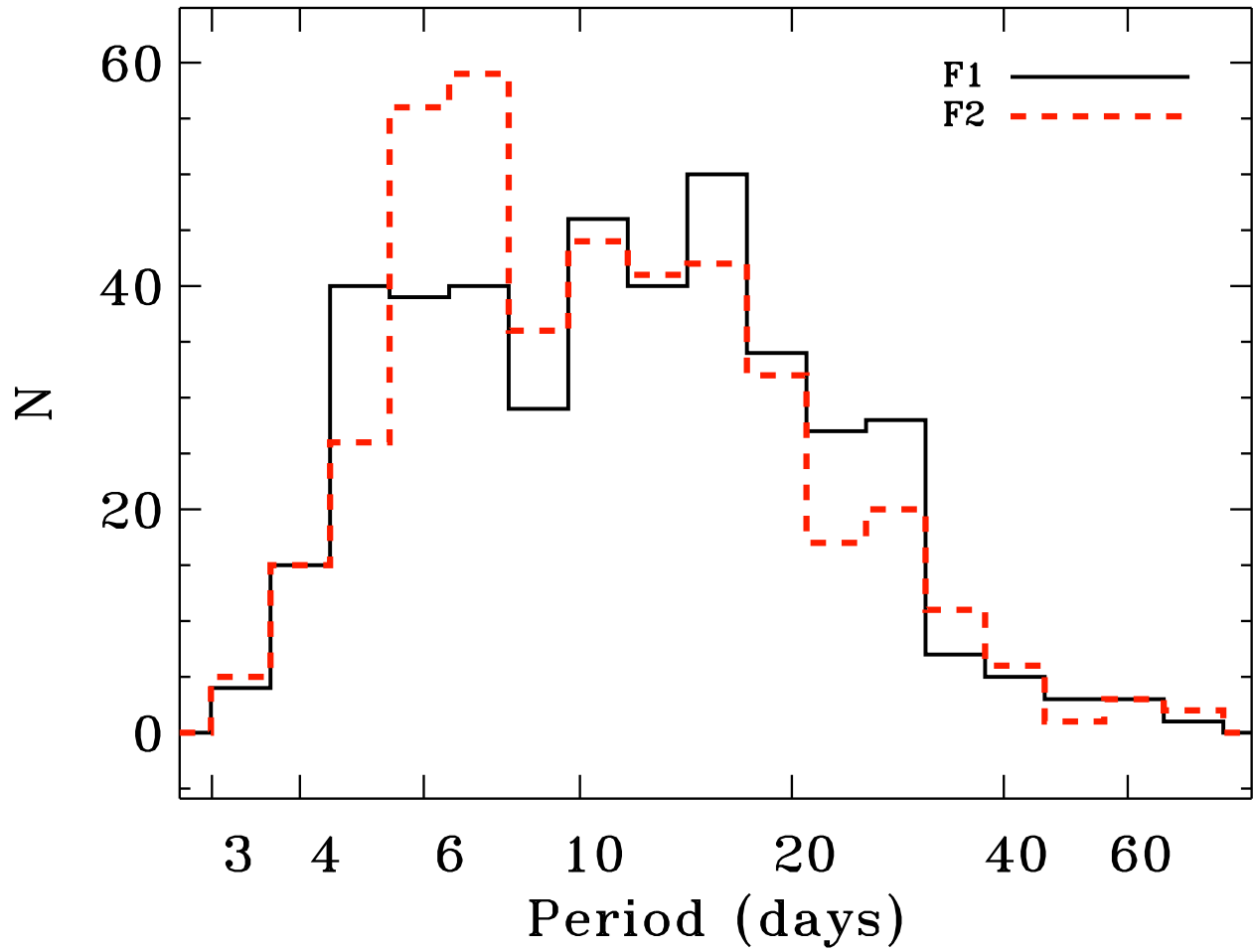


Fig. 9.— Distribution of periods in Field 1 (solid) and Field 2 (dashed) for the final Cepheid sample shown in Table 3. Figure discussed in §4.4.

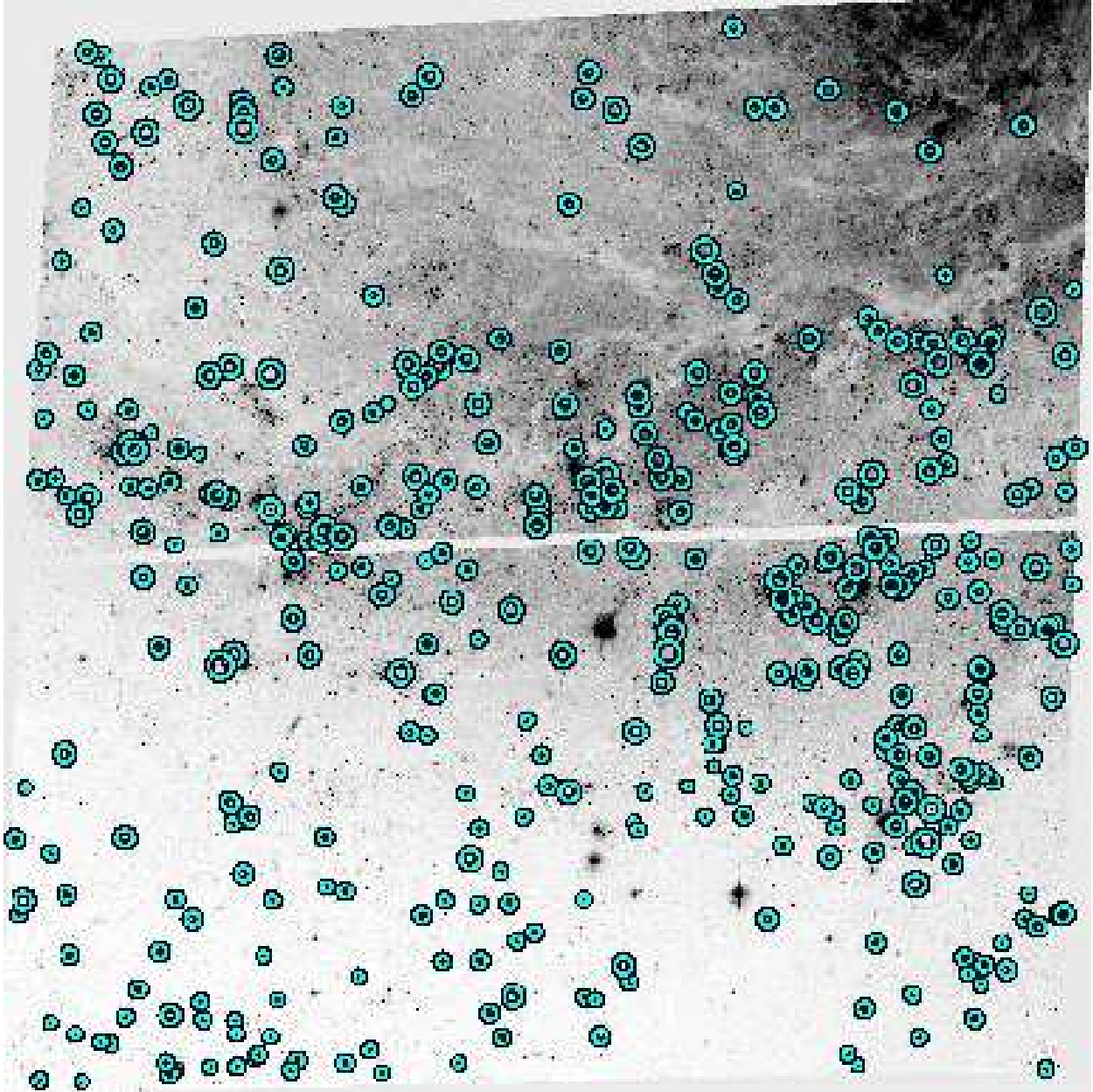


Fig. 10.— ISIS reference image of the HST ACS/WFC F555W data for Field 1 in M101. Cepheids from the final sample shown in Table 3 are marked by teal open circles. The area of each circle is proportional to the logarithm of the Cepheid’s period. The shortest and longest period Cepheids have periods of 3.2 days and 75.4 days, respectively. Figure discussed in §4.4.

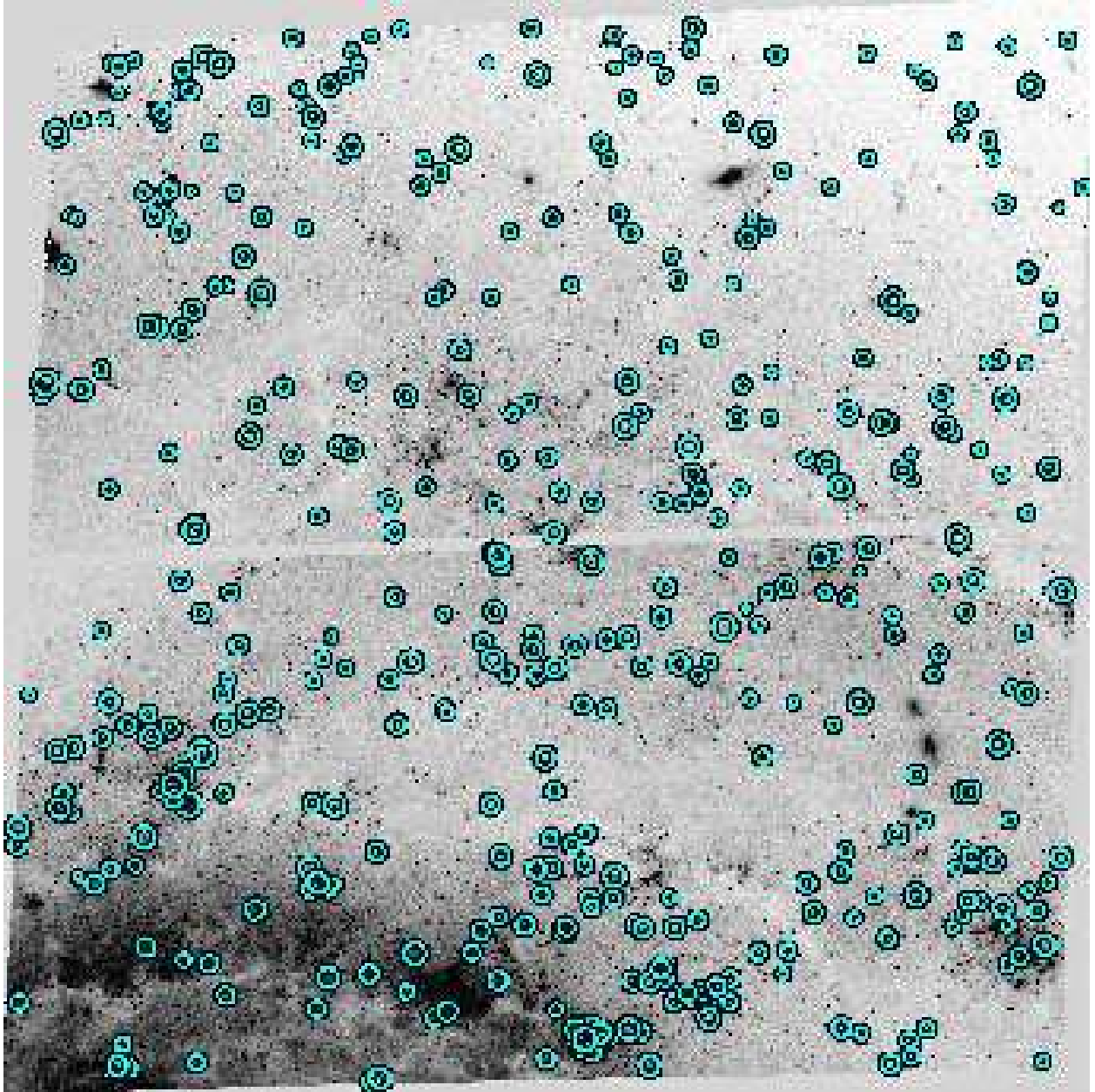


Fig. 11.— ISIS reference image of the HST ACS/WFC F555W data for Field 2 in M101. Cepheids from the final sample shown in Table 3 are marked by teal open circles. The area of each circle is proportional to the logarithm of the Cepheid’s period. The shortest and longest period Cepheids have periods of 3.0 days and 69.4 days, respectively. Figure discussed in §4.4.

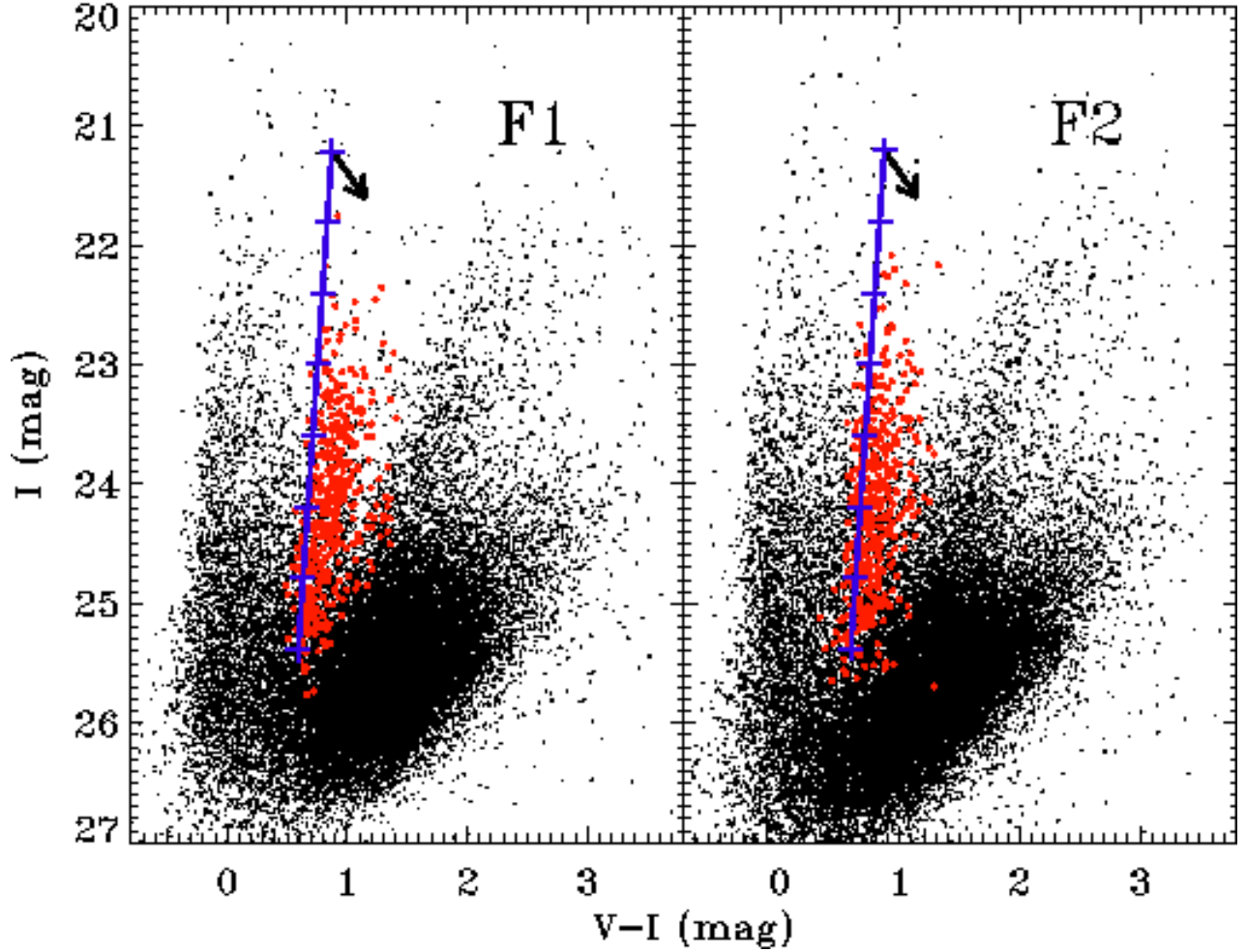


Fig. 12.— I versus $(V - I)$ color-magnitude diagram for Field 1 (left) and Field 2 (right), displaying every fifth source. The solid blue lines are the predicted position of the unreddened LMC P-L relations of Udalski et al. (1999a) for Cepheids of periods 4-100 days, shifted to the distance modulus fit in Fig. 16 and Fig. 17. The tick marks are every 0.2 log (days) along the P-L relation. The arrow indicates a reddening of $E(B - V) = 0.2$ mag. Red circles represent the final Cepheid sample presented in Table 6. Figure discussed in §4.4.

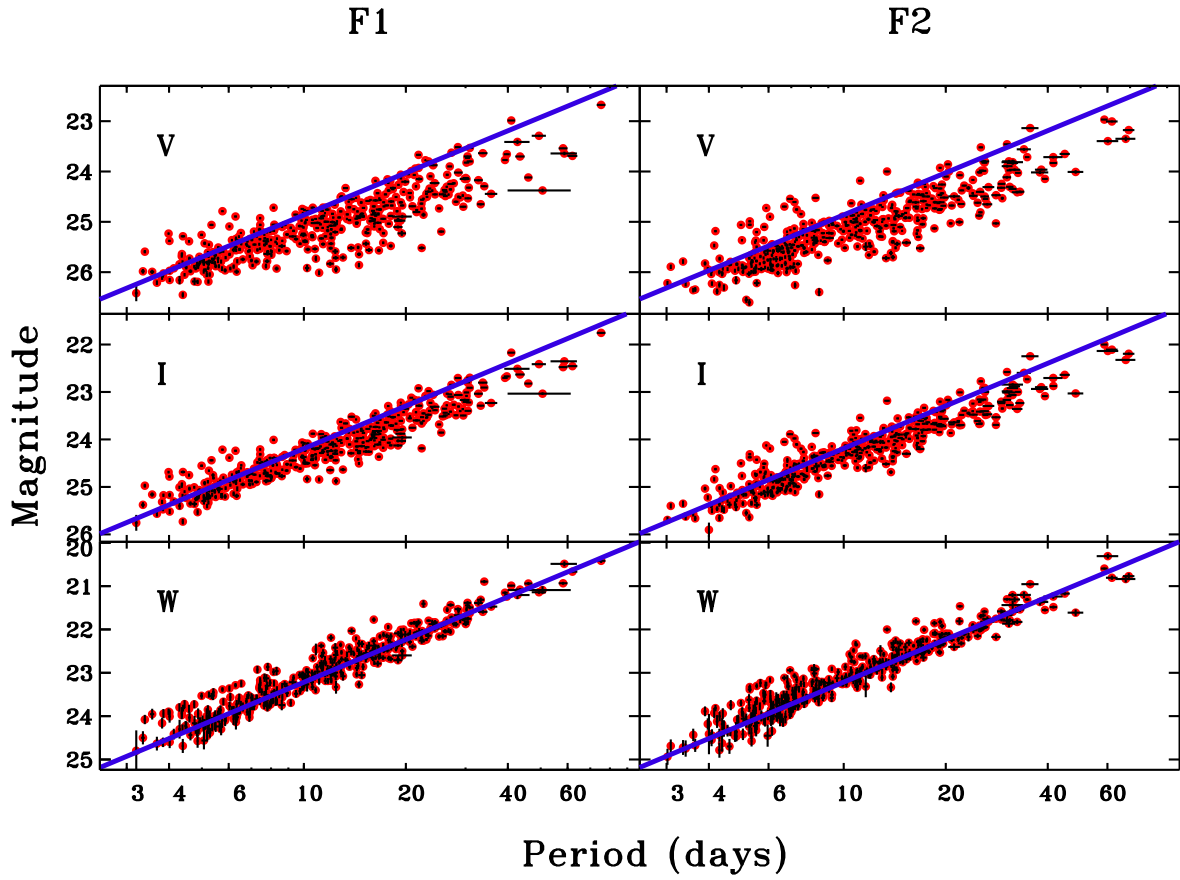


Fig. 13.— V , I and Wesenheit P-L relations for Field 1 (left) and Field 2 (right). The blue solid lines are the LMC P-L relations of Udalski et al. (1999a) shifted to the distance modulus fit in Fig. 16 and Fig. 17. Random errors for both period and magnitude are shown. Reddening can be seen in the V and I P-L relations. Figure discussed in §4.4.

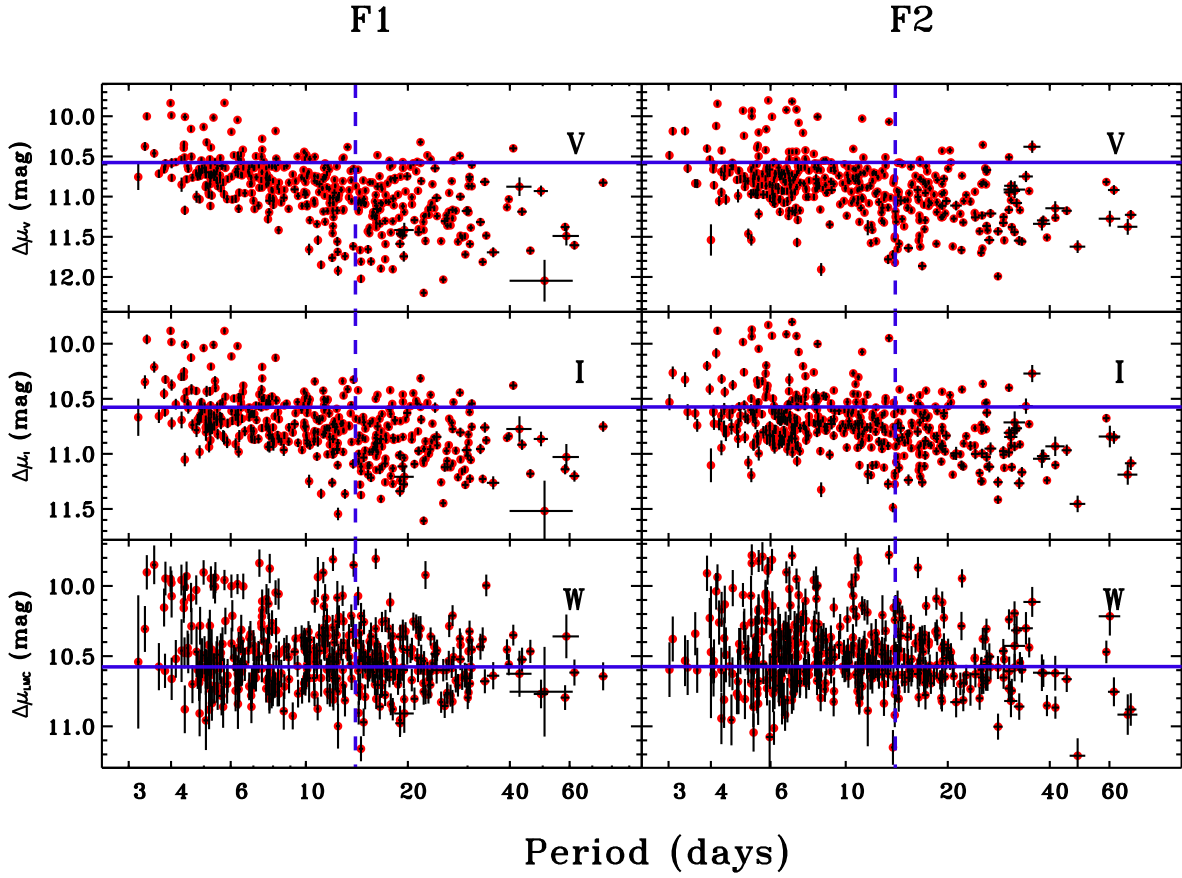


Fig. 14.— V , I and Wesenheit LMC relative distance moduli of the Cepheids as a function of period for Field 1 (left) and Field 2 (right). The vertical dashed blue line marks the minimum period cut used in each field to refine the final Cepheid sample used to determine the distance modulus. 155 Cepheids in Field 1 and 135 Cepheids in Field 2 have periods larger than the period cut. The horizontal solid blue line represents the distance modulus fit in Fig. 16 and Fig. 17. Random errors for both period and relative distance modulus are shown. Reddening can be seen in the V and I P-L relations for Cepheids with periods above the period cut. Figure discussed in §4.4.

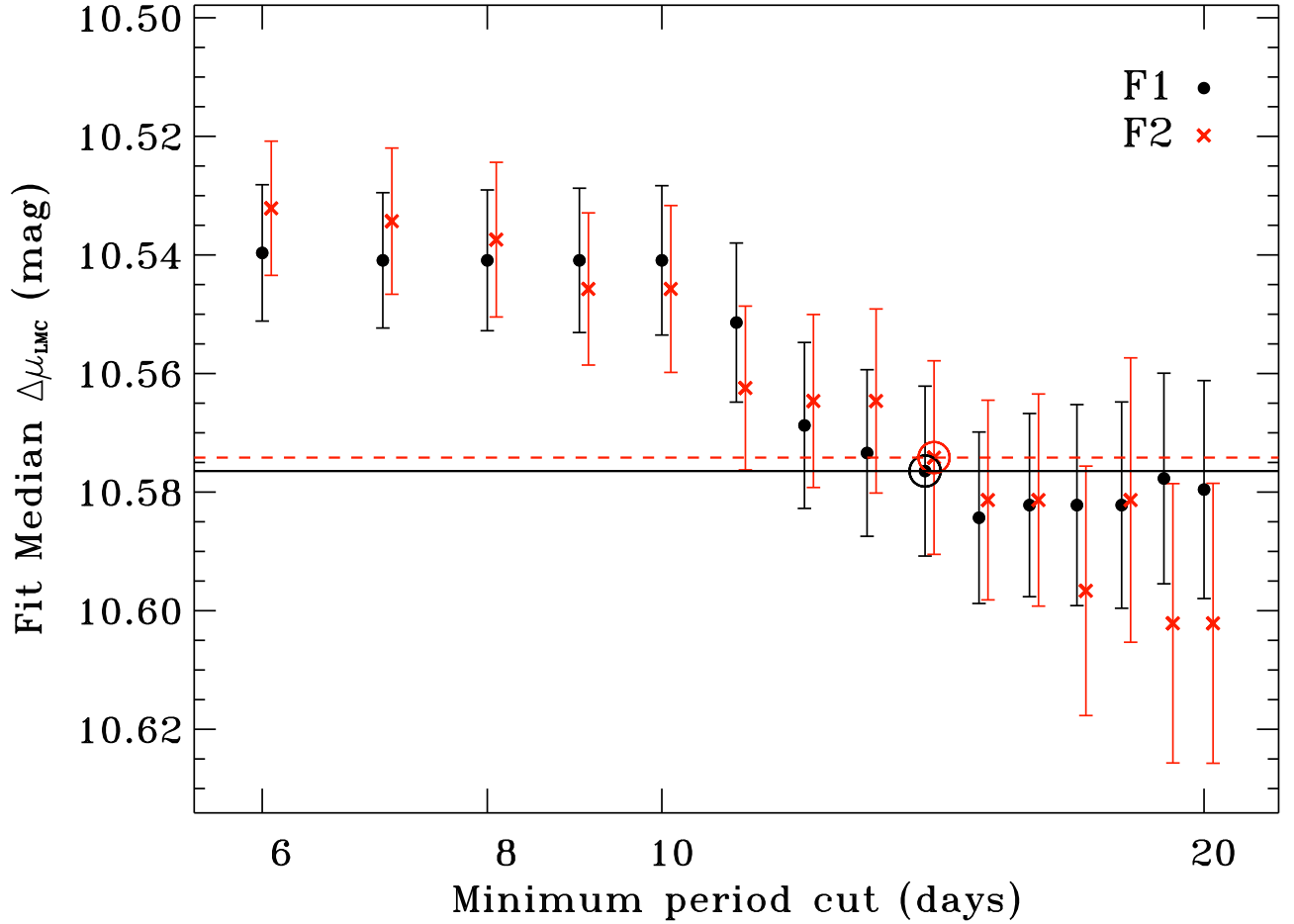


Fig. 15.— Median relative Wesenheit distance moduli as a function of the minimum period cut applied. Filled circles represent Field 1. Red crosses represent Field 2 and are shifted to higher periods by $0.01 \log(\text{days})$. The solid line and the dashed red line represents the median distance modulus for Field 1. Final choices for period cut are shown by open circles. 155 Cepheids in Field 1 and 135 Cepheids in Field 2 have periods larger than the period cut. The dashed line represents the median distance modulus at the period cut for Fields 1 and 2, respectively. Figure discussed in §5.1.

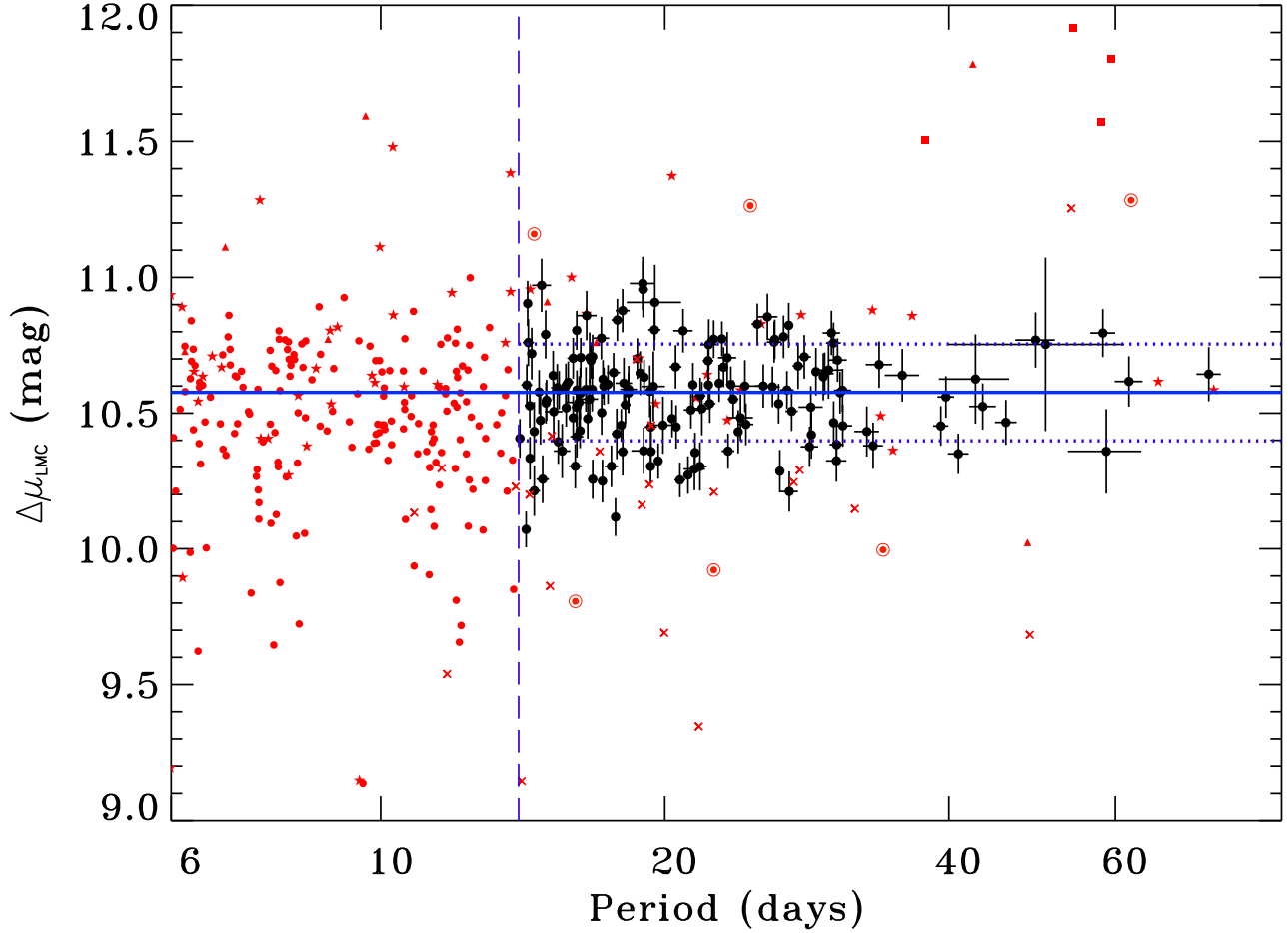


Fig. 16.— Relative Wesenheit distance moduli as a function of period for Field 1. Random errors are shown for Cepheids with periods larger than the period cut. Figure discussed in §5.1. **Filled Circles:** 155 Cepheids with periods larger than the period cut. **Solid line:** Median relative distance modulus. **Dotted line:** 1σ dispersion about the median in final Cepheid sample. **Dashed line:** Represents period cut. **Red Symbols:** Cepheids removed from various cuts. **Stars:** Amplitude ratio cut. **Triangles:** Blue blends cut. **Crosses:** Red blend or large extinction cut. **Squares:** Population II Cepheid or egregious outlier cut. **Red Circle:** Period cut. **Circled Red Point:** Iterative sigma clipping.

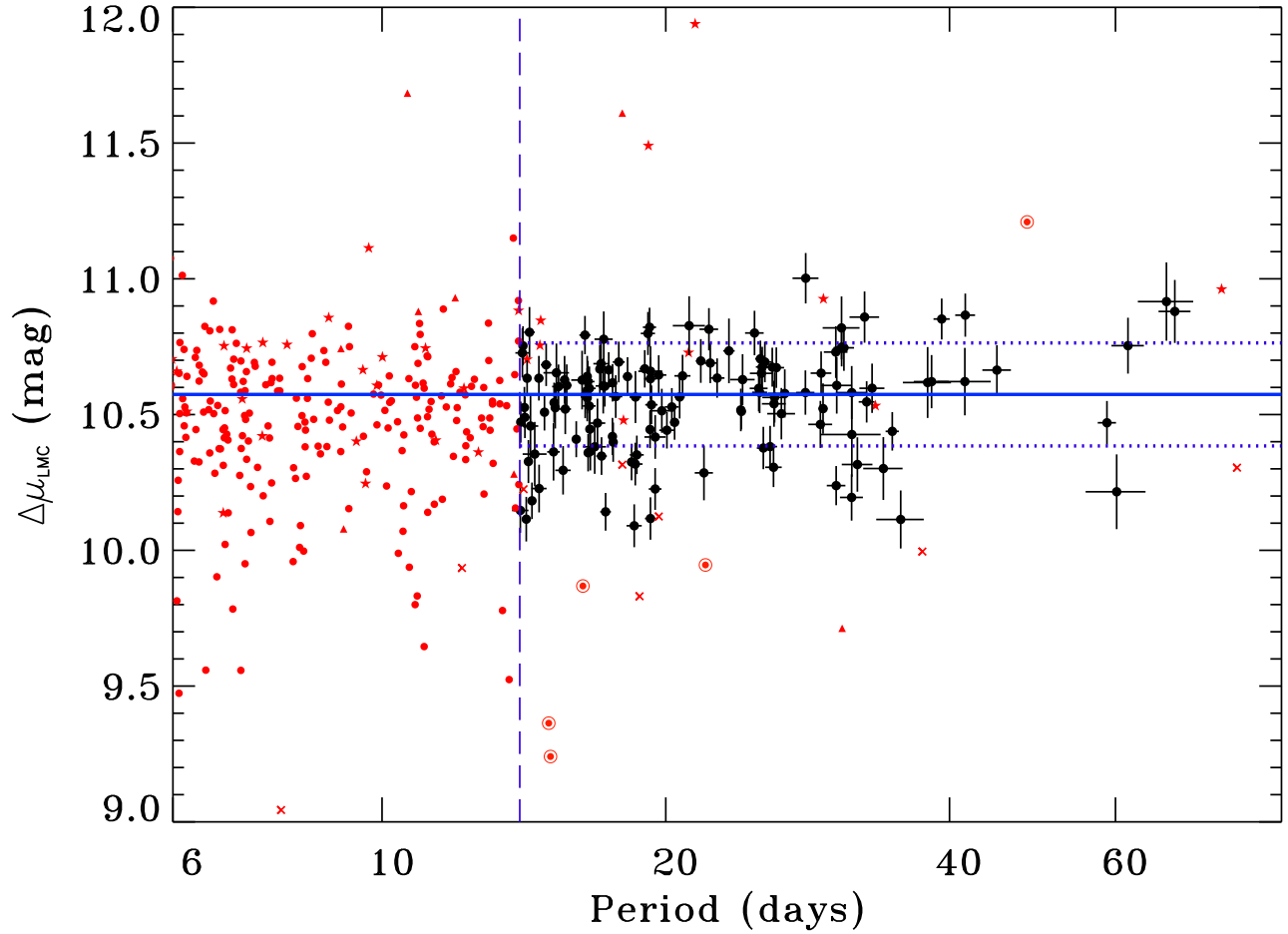


Fig. 17.— Relative Wesenheit distance moduli as a function of period for Field 2. Random errors are shown for Cepheids with periods larger than the period cut. Figure discussed in §5.1. **Filled Circles:** 135 Cepheids with periods larger than the period cut. **Solid line:** Median relative distance modulus. **Dotted line:** 1σ dispersion about the median in final Cepheid sample. **Dashed line:** Represents period cut. **Red Symbols:** Cepheids removed from various cuts. **Stars:** Amplitude ratio cut. **Triangles:** Blue blends cut. **Crosses:** Red blend or large extinction cut. **Squares:** Population II Cepheid or egregious outlier cut. **Red Circle:** Period cut. **Circled Red Point:** Iterative sigma clipping.

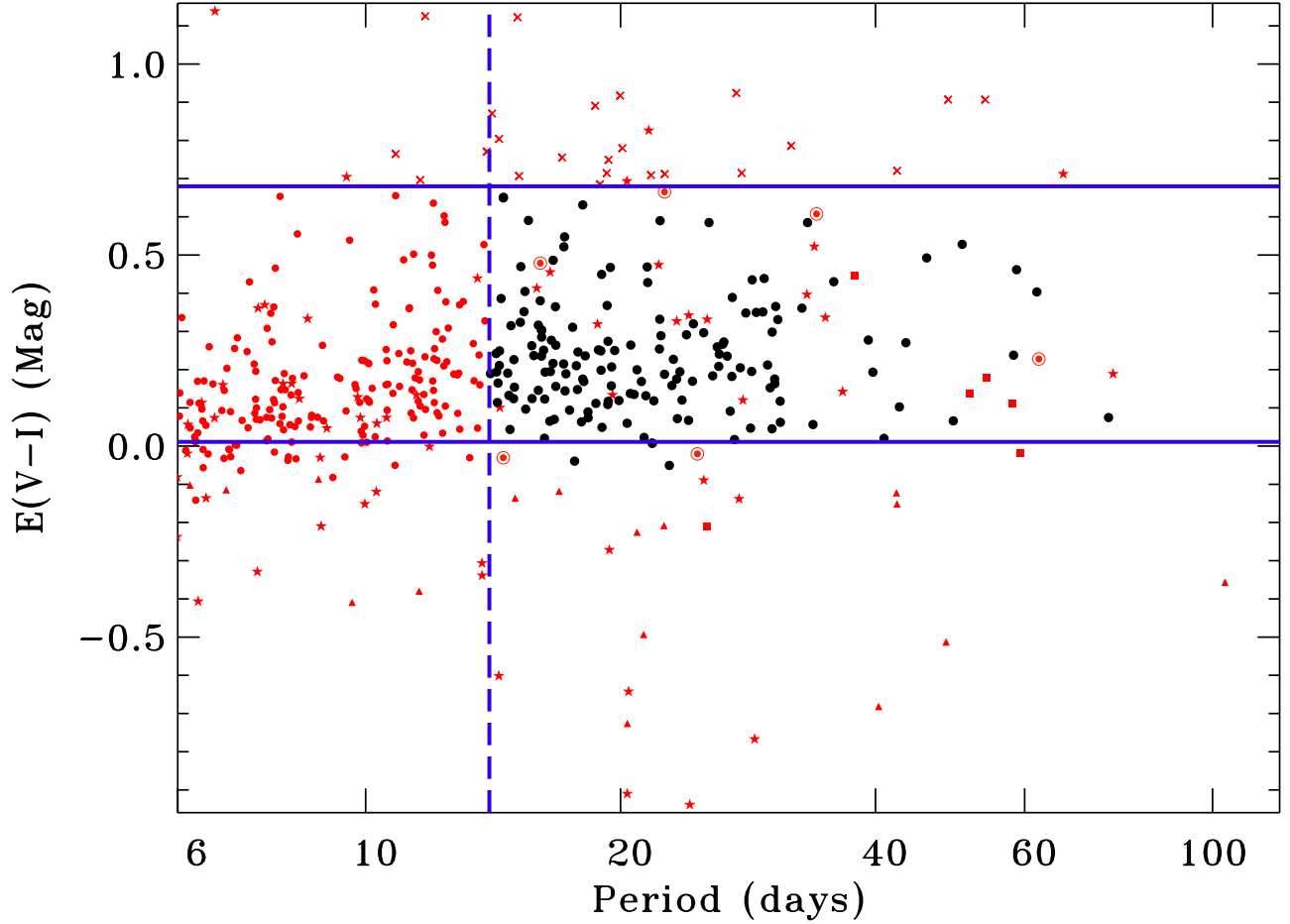


Fig. 18.— $E(V-I)$ as a function of period for Field 1. **Filled Circles:** 155 Cepheids with periods larger than the period cut. **Solid line:** $E(V-I)$ values where the large extinction and blue blend cuts were applied. **Vertical Dashed line:** Represents period cut off. **Red Symbols:** Cepheids removed from various cuts. **Stars:** Amplitude ratio cut. **Triangles:** Blue blends cut. **Crosses:** Red blend or large extinction cut. **Squares:** Population II Cepheid or egregious outlier cut. **Red Circle:** Period cut. **Circled Red Point:** Iterative sigma clipping. Figure discussed in §5.1.

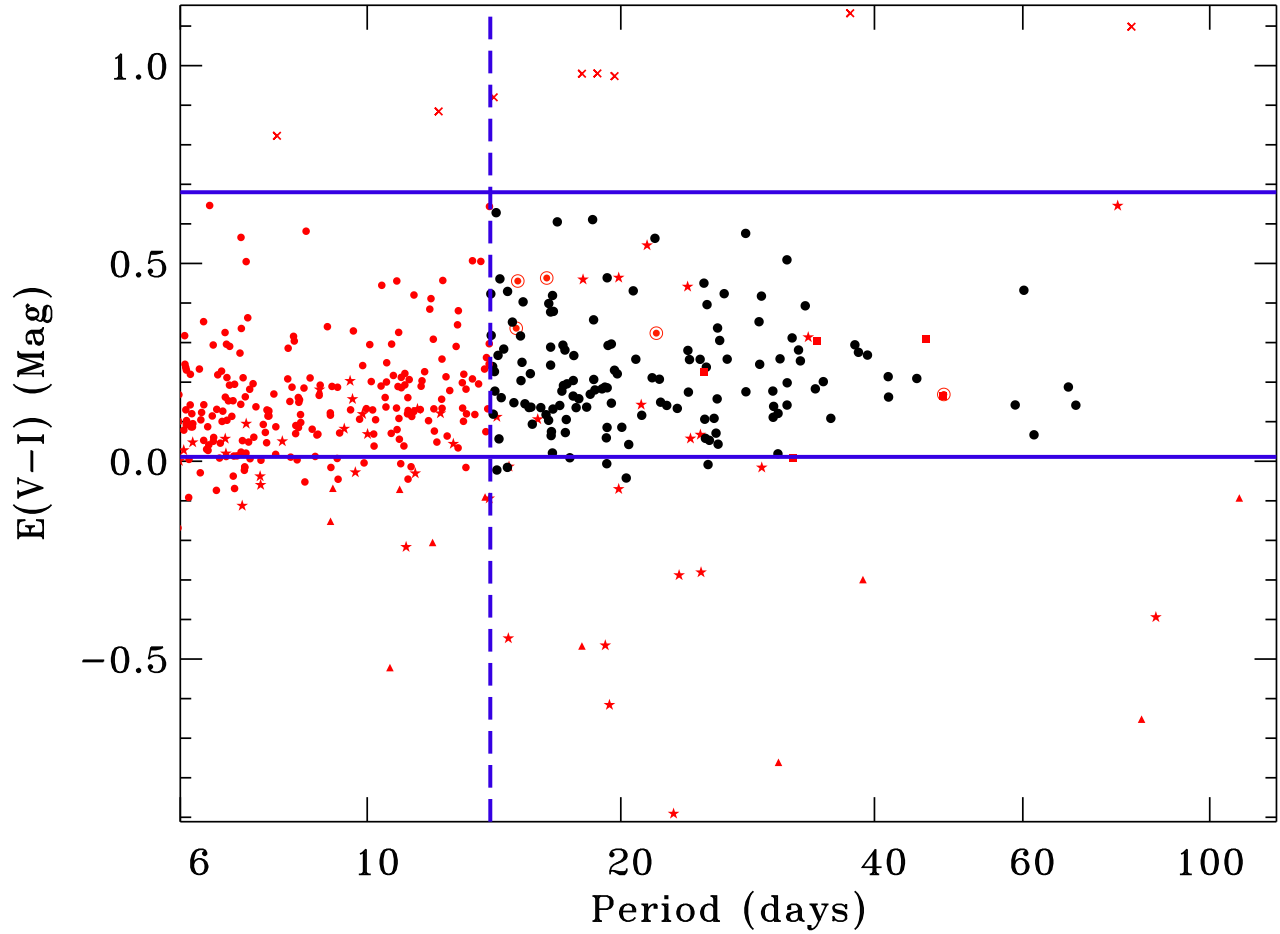


Fig. 19.— $E(V - I)$ as a function period for Field 2. **Filled Circles:** 135 Cepheids with periods larger than the period cut. **Solid line:** $E(V - I)$ values where the large extinction and blue blend cuts were applied. **Vertical Dashed line:** Represents period cut off. **Red Symbols:** Cepheids removed from various cuts. **Stars:** Amplitude ratio cut. **Triangles:** Blue blends cut. **Crosses:** Red blend or large extinction cut. **Squares:** Population II Cepheid or egregious outlier cut. **Red Circle:** Period cut. **Circled Red Point:** Iterative sigma clipping. Figure discussed in §5.1.

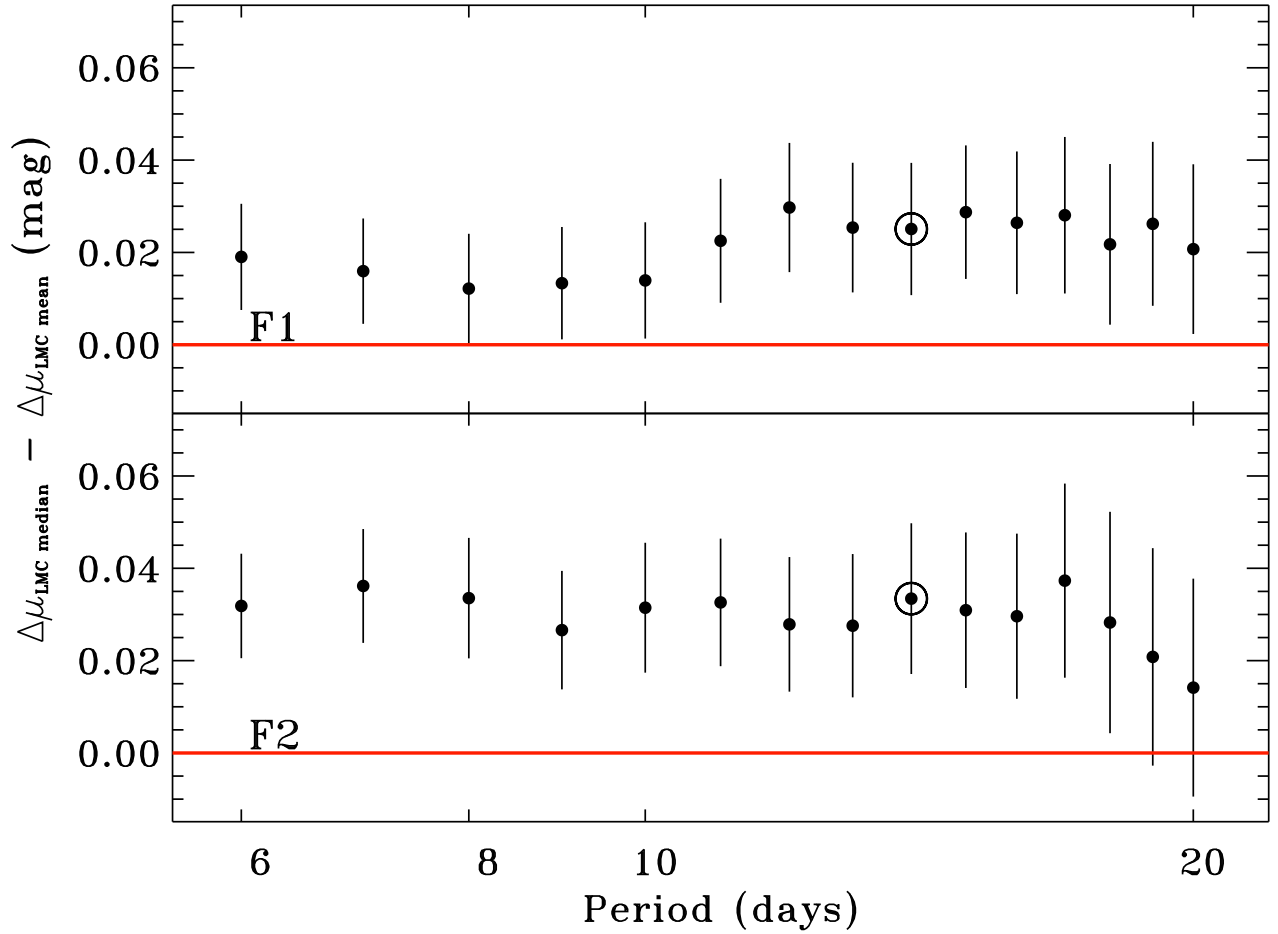


Fig. 20.— Difference between median and mean relative Wesenheit distance moduli as a function minimum period cut applied. Top: Field 1. Bottom: Field 2. Solid red line is at 0 to guide the eye. Errors estimates shown are the quadrature addition of the scatter about the median and the scatter about the mean. Figure discussed in §5.1.

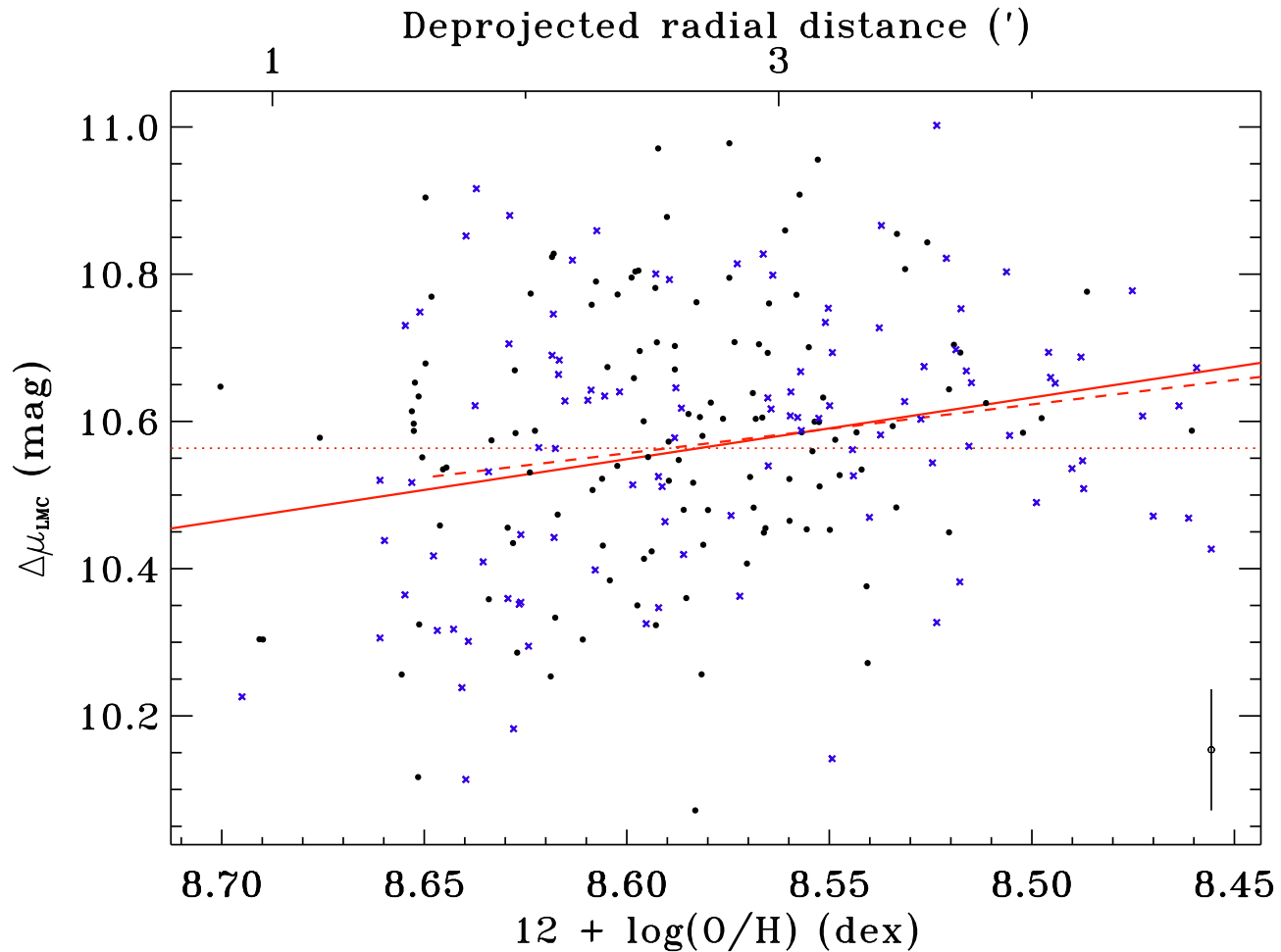


Fig. 21.— Metallicity dependence of the relative Wesenheit distance modulus. Filled circles and blue crosses represent Cepheids in the refined sample in Fields 1 and 2, respectively. The solid red best-fit line is shown with a slope of $-0.84 \pm 0.22_r \pm 0.07_s$ mag dex $^{-1}$. The dotted red best-fit constant is shown for reference. The dashed red best-fit line to a restricted sample of Cepheid with $12 + \log(\text{O}/\text{H}) < 8.65$ dex is shown with a slope of $-0.66 \pm 0.25_r \pm 0.05_s$ mag dex $^{-1}$. At $12 + \log(\text{O}/\text{H}) = 8.5$ dex, the LMC relative distance modulus of M101 is $\Delta\mu_{\text{LMC}} = 29.04 \pm 0.02_r \pm 0.04_s$. The error bar on the open circle in lower right displays the average individual random uncertainties. Figure discussed in §5.2.

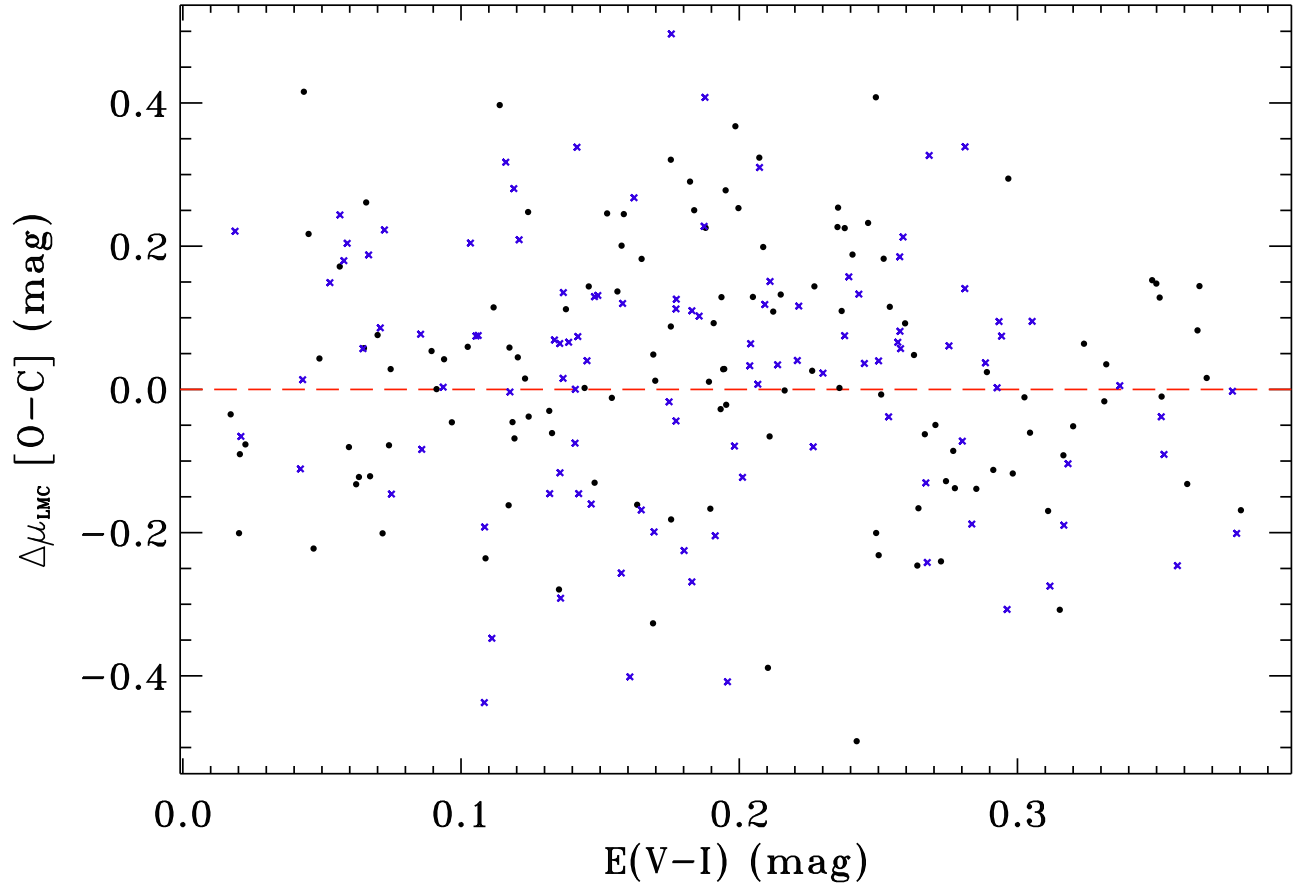


Fig. 22.— Residuals about the best-fit metallicity relation shown in Fig. 21. Filled circles and blue crosses represent Cepheids in the refined sample in Fields 1 and 2, respectively. Dashed red line shown at $\Delta\mu_{\text{LMC}}[O - C] = 0$ to aid the eye. Figure discussed in §5.2.

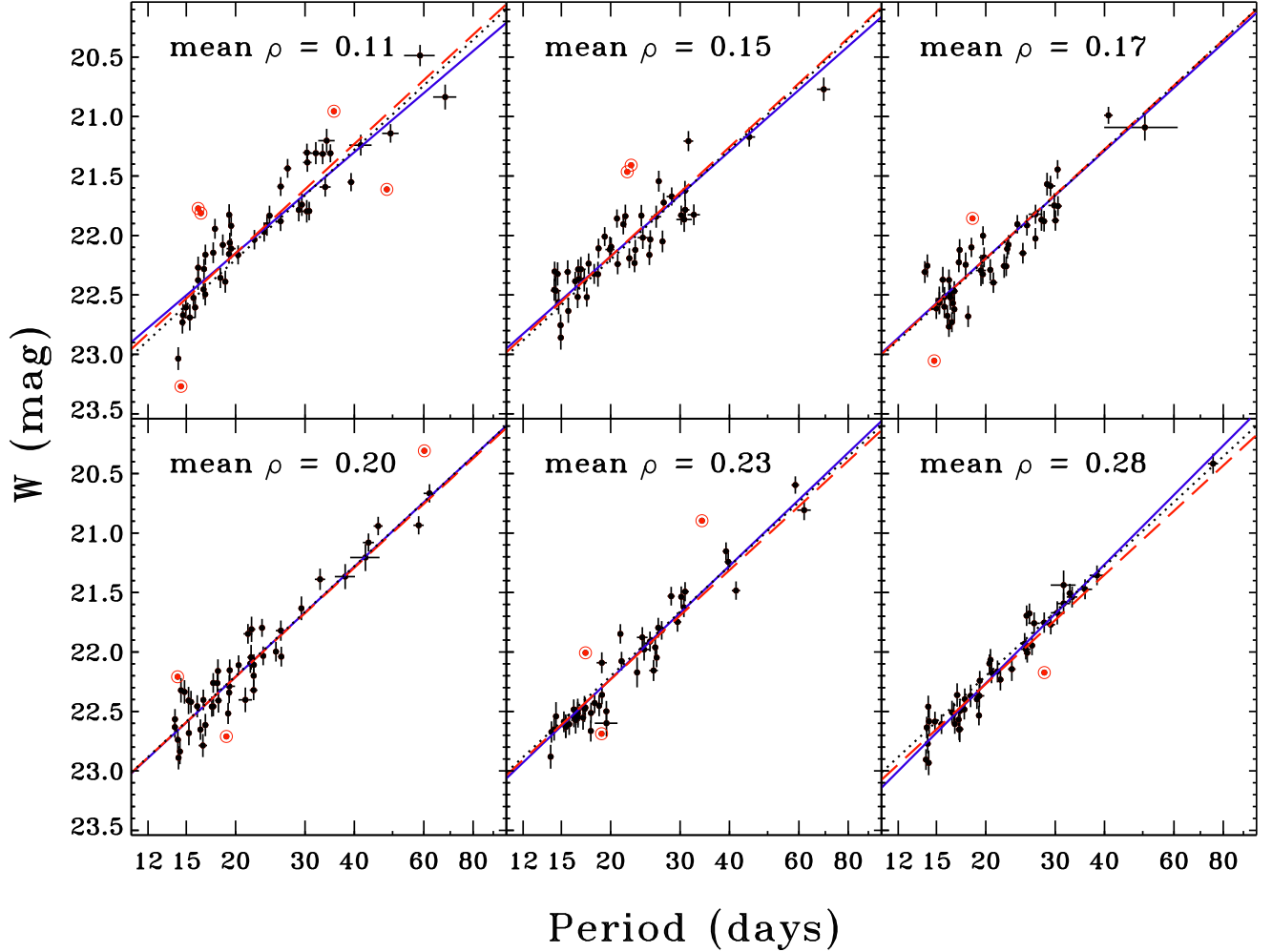


Fig. 23.— Wesenheit P-L relations with equal numbers of Cepheids in bins of deprojected radius. Filled circles represent Cepheids selected in §4.4 with an additional minimum period cut of 14 days. The dotted black line indicates fit Wesenheit P-L relation with no variation as function of deprojected radius (Model 1). The dashed red line represents the best-fit Wesenheit P-L with constant a slope and a linearly varying zero-point as a function of deprojected radius (Model 2). The solid blue line is the best-fit Wesenheit P-L allowing linear variations in the slope and zero-point as a function of deprojected radius (Model 4). Cepheids were removed by iterative sigma clipping from Model 1 and are represented by red points encircled by red rings. The mean Cepheid deprojected isophotal radius fraction is shown for each frame. Fit parameters shown in Table 9. Figure discussed in §6 and §9.

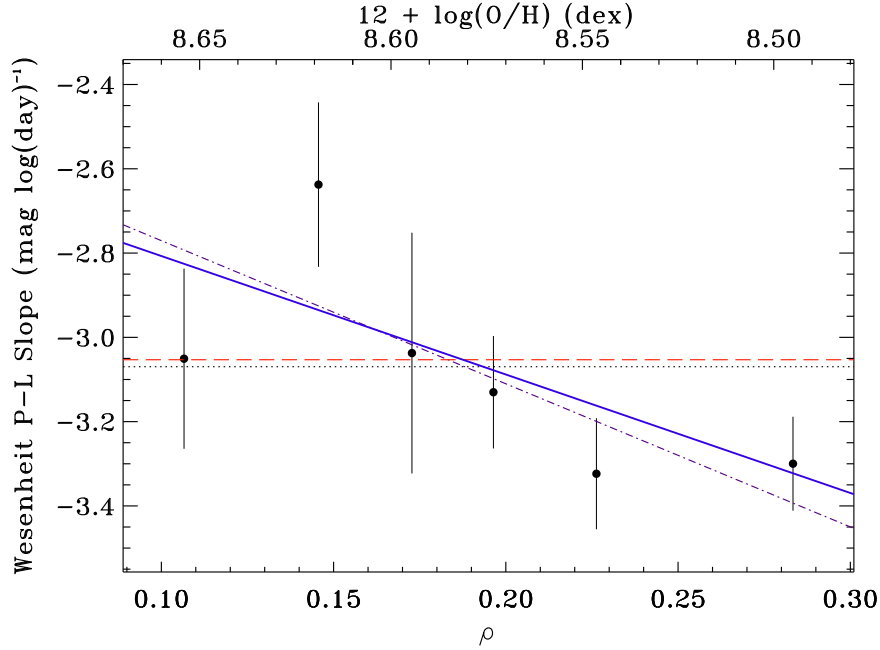


Fig. 24.— The best-fit slope of the Wesenheit P-L relation as a function of fractional isophotal radius. The dotted black line indicates fit Wesenheit P-L relation with constant slope and zero-point (Model 1). The dashed red line represents fit Wesenheit P-L with constant slope and linearly varying zero-point as a function of deprojected radius (Model 2). The dot dashed purple line indicates fit Wesenheit P-L with constant zero-point and linear varying slope as a function of deprojected radius (Model 3). The dashed red line represents fit Wesenheit P-L with linear varying slope and zero-point as a function of deprojected radius (Model 4). The filled black dots represent the slopes of the individually fit Wesenheit P-L relations for smaller samples shown in Fig. 23 with error bars determined using bootstrap re-sampling. It is important to note that these individually fit sub-samples are plotted for comparison purposes only. Figure discussed in §6.

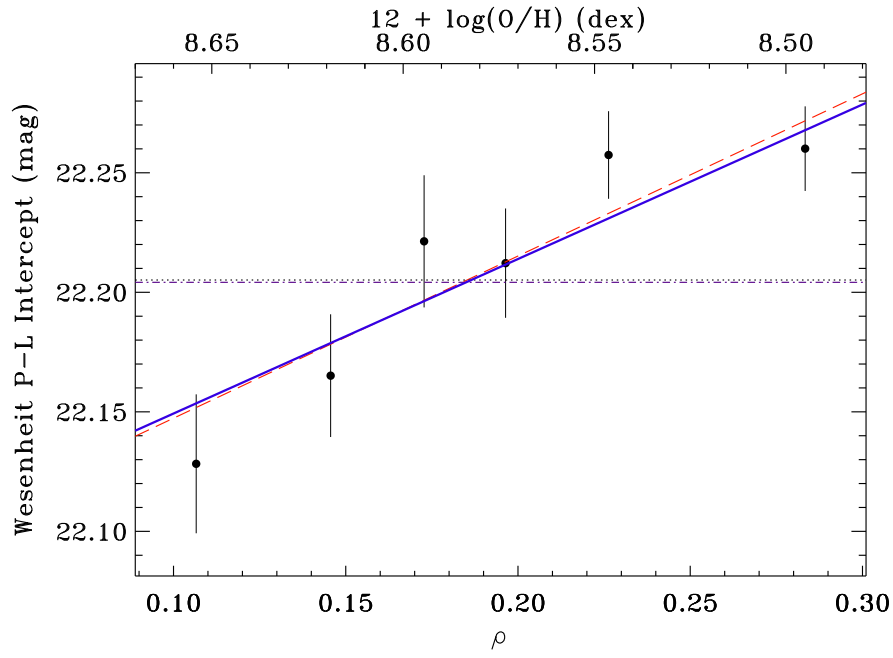


Fig. 25.— Same as Fig. 24 but showing the Wesenheit P-L zero-point as a function of fractional isophotal radius. Figure discussed in §6.

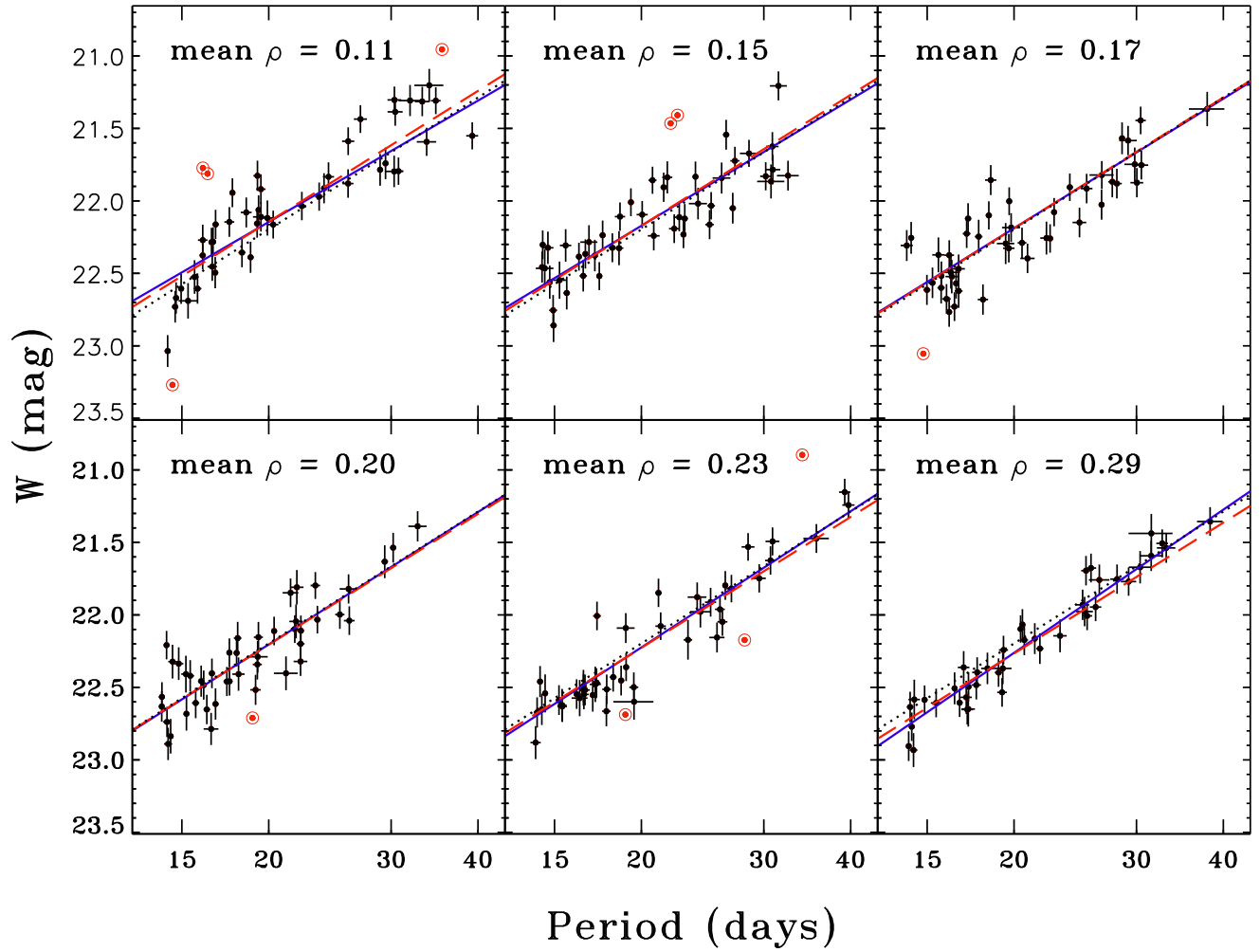


Fig. 26.— Same as Fig. 23 but for the sample Cepheids with a maximum period cut of $P < 40.0$ days. Fit parameters shown in Table 9. Figure discussed in §6 and §9.

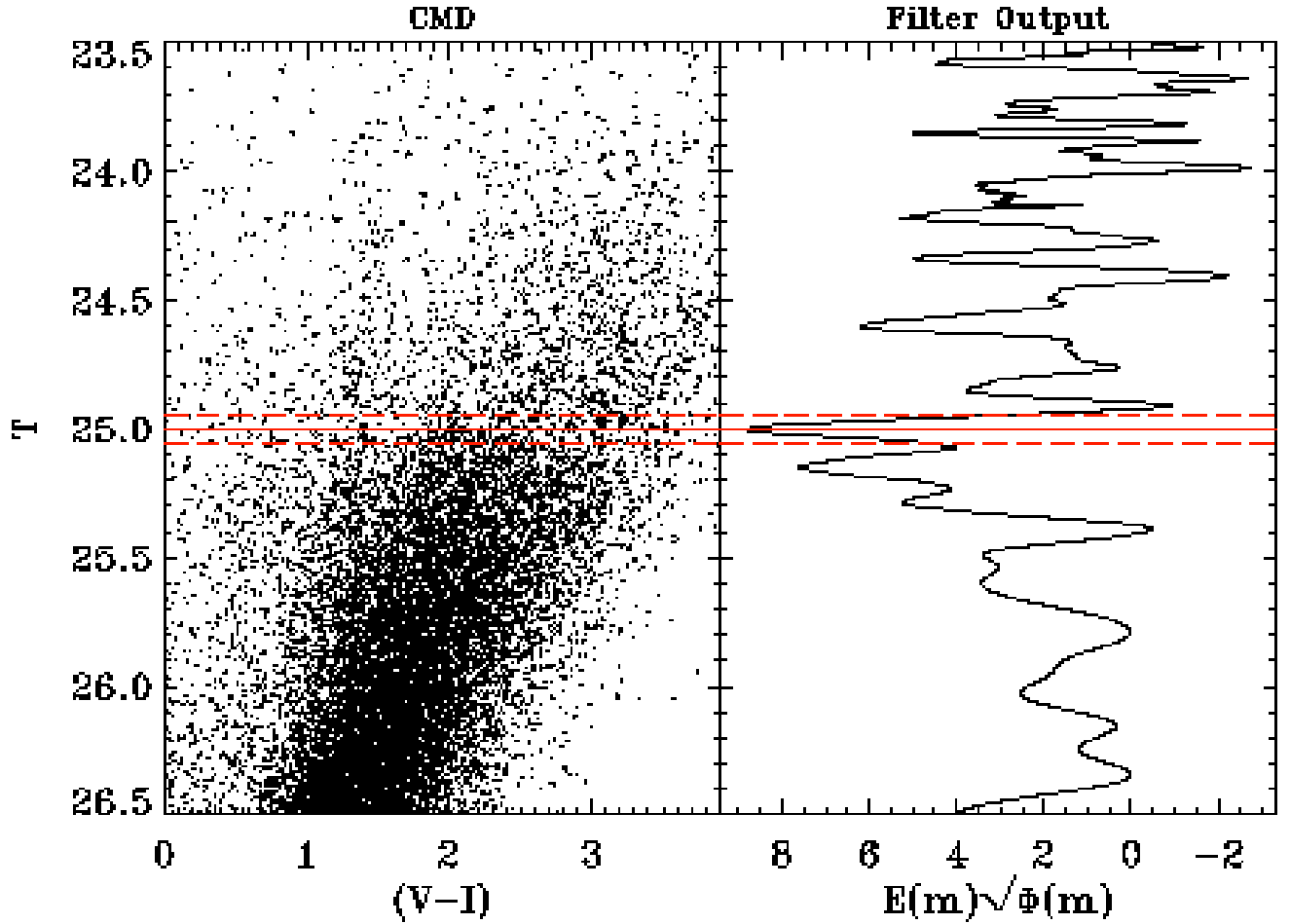


Fig. 27.— Determination of the T TRGB magnitude for M101 where $T = I - 0.20[(V - I) - 1.5]$ (Madore et al. 2009). Left: T vs. $(V - I)$ color-magnitude diagram for sources 4.75 from the galactic center of M101. Right: Edge detection function $E(m)\sqrt{\phi(m)}$, where the maximum value at 25.00. Solid red line: Represents the maximum value of the edge detection function. Dashed red lines: Represent estimated uncertainty of the edge detection based on bootstrap re-sample described in §7.

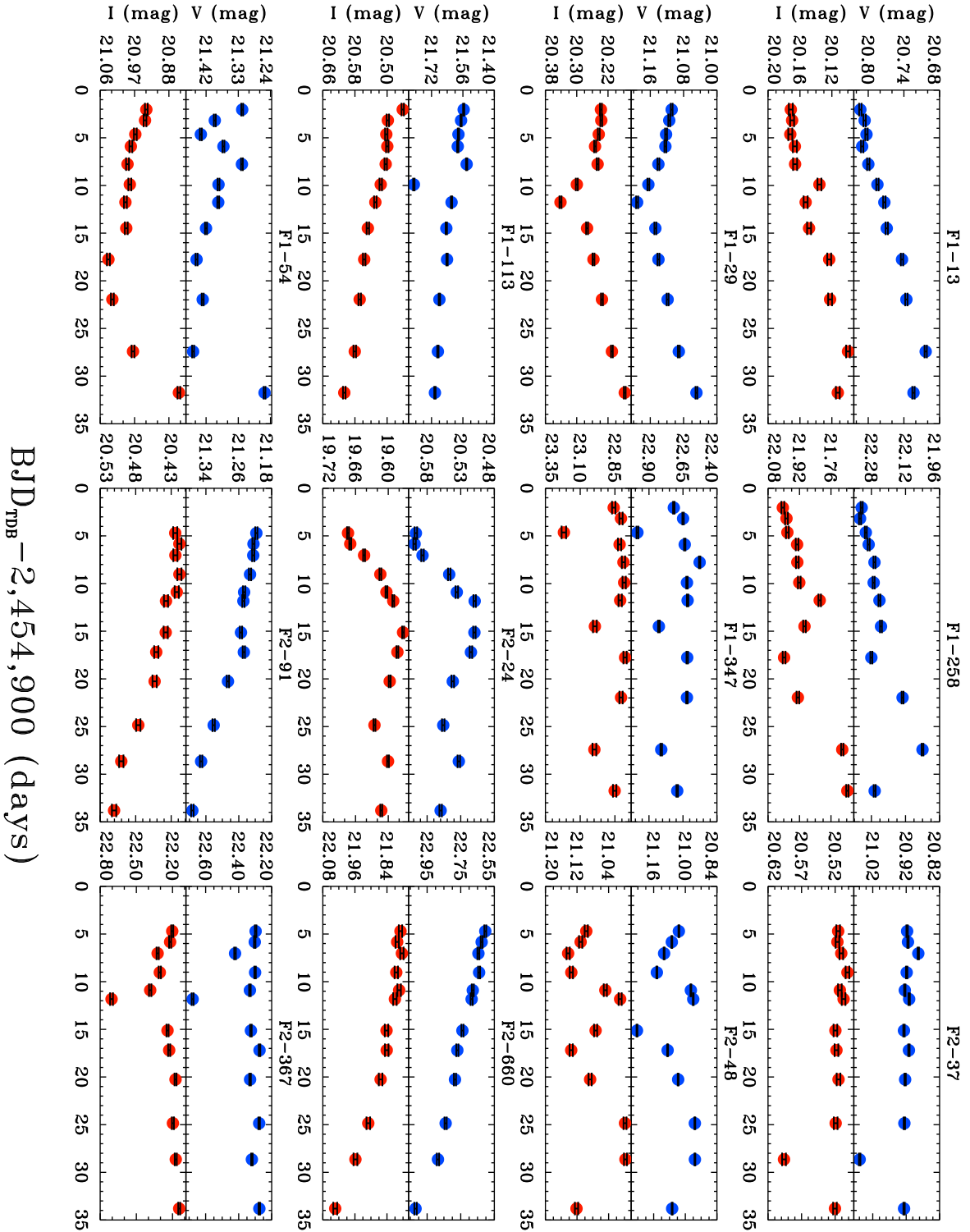


Fig. 28.— Light curves of interesting luminous variable objects. Blue (top): V filter light curves. Red (bottom): I filter light curves. Photometric errors are shown but usually smaller than the points. Figure discussed in §8.

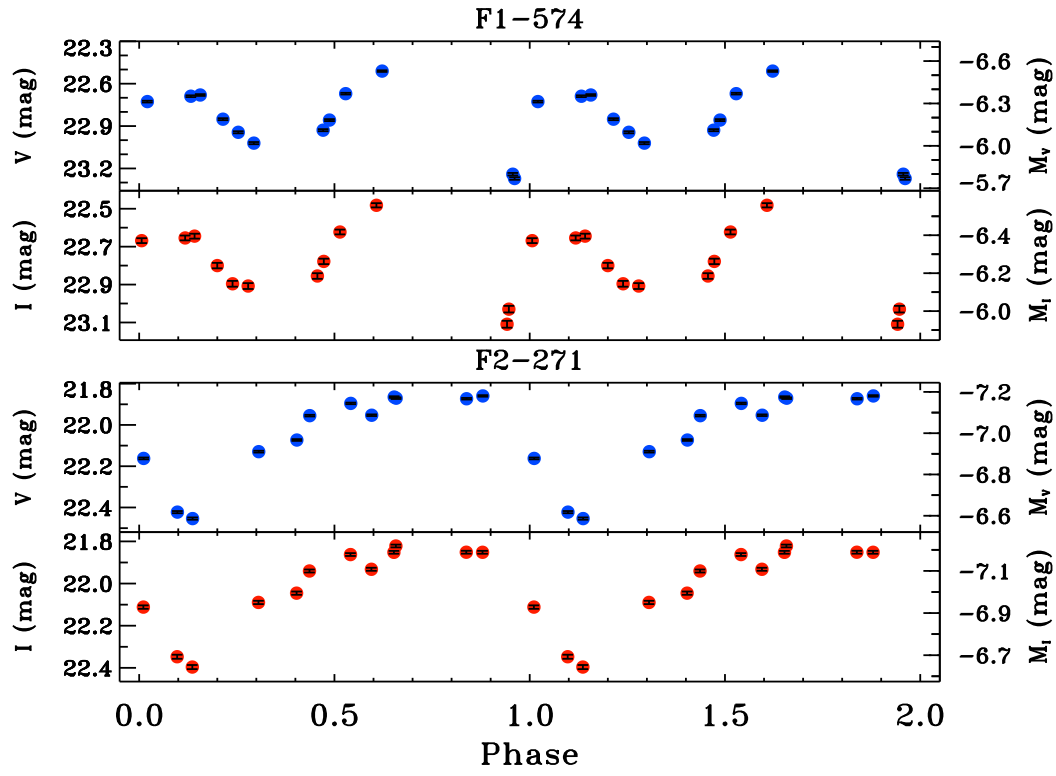


Fig. 29.— Object F1-574 (top) and F2-271 (bottom) which show possible periodic behavior with $P = 0.508$ days and $P = 10.78$ days respectively. Absolute magnitudes on the right side of the figure assume our Cepheid distance modulus and make no reddening correction. Figure discussed in §8.

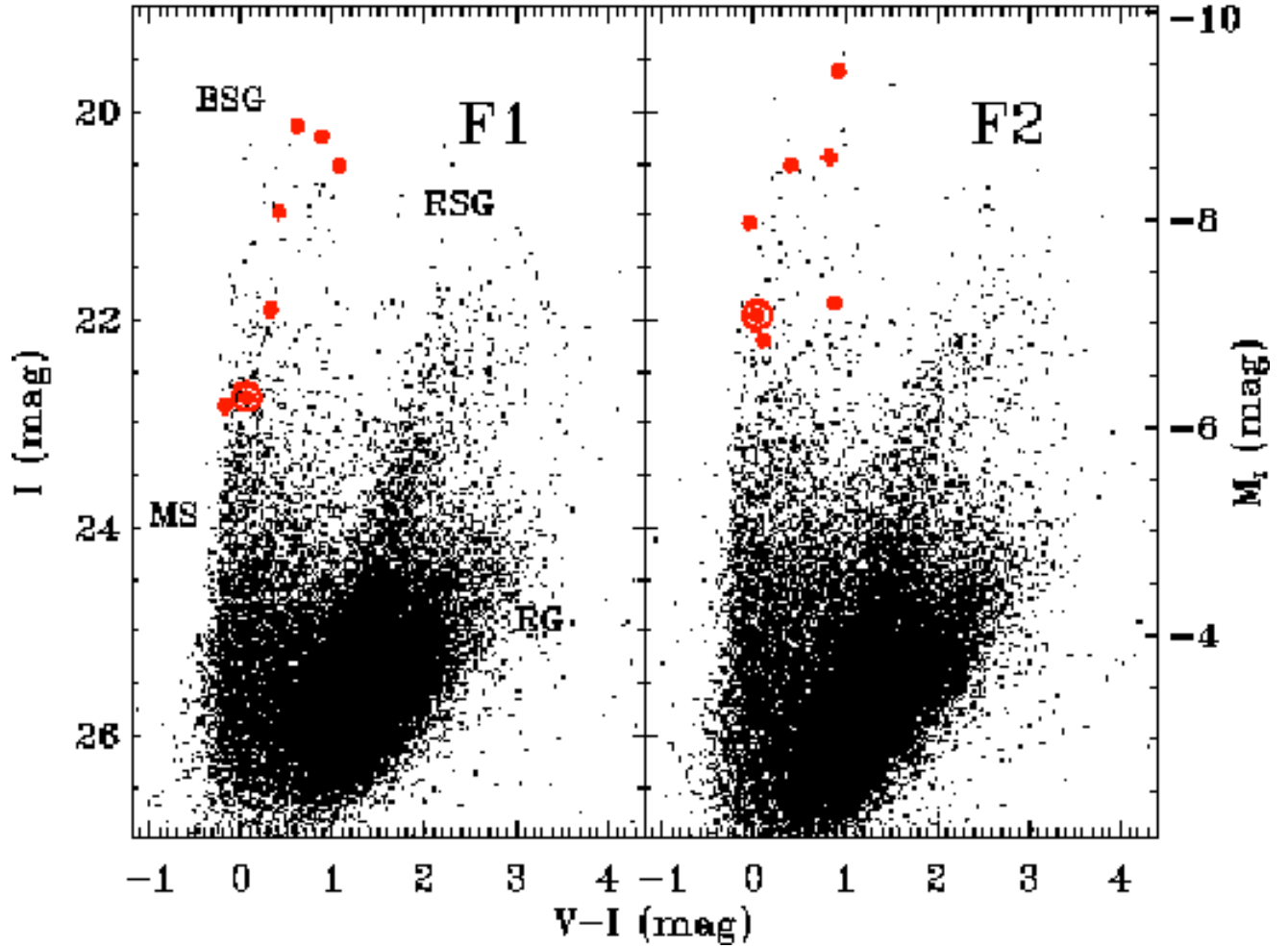


Fig. 30.— I vs. $(V - I)$ color-magnitude diagram for M101 for Field 1 (left) and Field 2 (right) displaying every fifth source. Red circles represent luminous variable object seen in Fig. 28 and Fig. 29. Red annuli mark the possible periodic objects. MS labels the location of the main sequence. BSG labels the location of blue super giants. RSG labels the location of red super giants. RG labels the location of red giants. Absolute magnitudes on the right side of the figure assume our Cepheid distance modulus and make no reddening correction. Figure discussed in §8.